FACULTY OF SCIENCE
UNIVERSITY OF COPENHAGEN

Master's thesis

Investigating the Nature of Damped Lyman-α Absorbing Galaxies

Rikke Lund Saust
Email: saust@dark-cosmology.dk

Submitted: June 30, 2014

Supervisor
Lise Christensen
Email: lise@dark-cosmology.dk

Dark Cosmology Centre
Niels Bohr Institute
University of Copenhagen

Abstract

This thesis focuses on investigating the physical conditions in galaxies as absorbers. A part of the thesis focuses on the Damped Lyman-α Absorbing systems, DLAs, which give important insights into the properties of galaxies, especially at high redshifts. A sample of 85 quasars observed with X-shooter on the Very Large Telescope has been searched for DLAs. This has resulted in identification of 33 high redshift DLAs. From the important property that the metallicity is related to the kinematics of DLAs, a mean metallicity for the DLA sample was found to be [M/H]=-1.8 dex by measuring the equivalent width of SiII 1526. DLAs are high column density neutral gas absorbers and contribute significantly to the cosmological mass density of neutral gas, which is connected to the star formation in galaxies. In order to contribute to previous studies of the cosmological mass density of neutral gas for DLAs, Ω_g^{DLA}, it was estimated for a sub-sample of the identified high redshift DLAs. The result is Ω_g^{DLA}=0.00167 $\pm$ 0.00069 at a redshift interval of $z = [3.22, 4.47]$, consistent with previous studies.

Another part of the thesis focuses on two low redshift galaxies(NGC-4193 and UGC-08066) near the sight-line of background quasars. Observations with long-slit spectra which cover both quasar and galaxy have been processed and analysed. Via emission line diagnostics the metallicity was measured across the galaxies and the radial metallicity gradients were found to be quite flat. Given that the metallicities was found to be around solar values, it is predicted that solar metallicity absorbing systems might be seen in the background quasar spectra. However, this has to be confirmed with ultra-violet data of the quasars. The line diagnostics also showed sign of shock ionization, possibly explained by bar shocks.

Contents

1 Lyman Alpha Absorbing Clouds

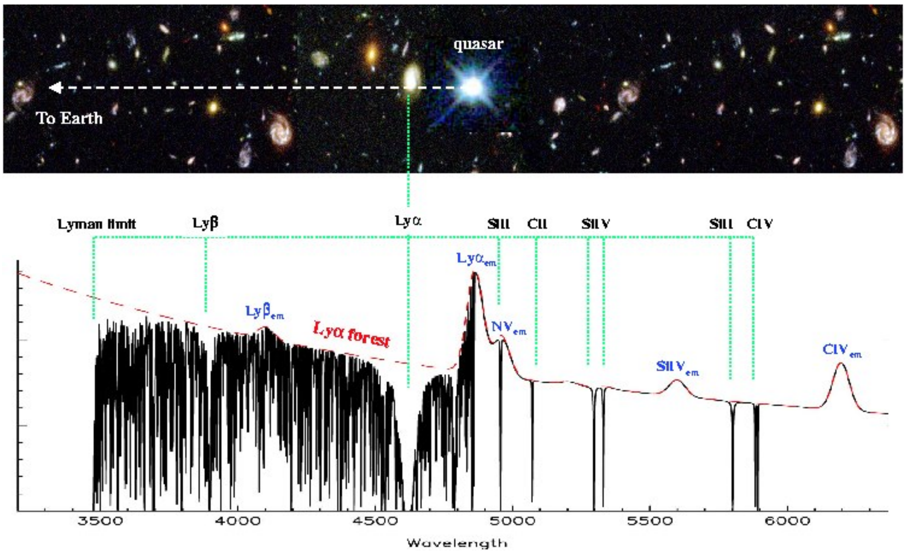

Figure 1: This illustration is a good example of a quasar spectrum which show absorption from intervening matter. The upper panel show the straight path which the quasar light follows towards the Earth. As seen there is an intervening galaxy, but besides this large absorber the inter galactic medium will also absorb. The lower panel show a spectrum of a high redshift quasar with the dashed red line indicating the unabsorbed spectrum. From the quasar Lyman-α line and bluewards the interaction with the intervening media is clearly seen. It is dominated by both the Lyman-α forest and the damped Lyman-α absorber, DLA. The metal lines and the Lymanβ DLA lines at the same redshift is shown with the cyan dotted lines. This figure is from `http://enki.phyast.pitt.edu/qso_abs.html`

.

Light from a bright extragalactic source heading towards the Earth will go through absorbing media on the way. Dust and gas in the intergalactic medium and interstellar media of other galaxies will then interact with the photons. The photons will scatter or be absorbed and imprints of the intervening material between the observer and the luminous source will be visible in the source spectrum, see figure 1. This is especially evident for high redshift luminous extragalactic sources. These sources might be the afterglow of a Gamma Ray Burst, GRB, or a quasar, QSO, which both were common in the early universe. The high redshift/long travel distance means that the light is more likely to pass through high absorbing media. In the ultra-violet and optical part of the electromagnetic spectrum a lot of the absorption is due to media of neutral hydrogen atoms, HI. HI mainly absorb via photoionization. The most likely/dominant excitation of HI is from the ground state to the first excitation state - the Lyman-α, Lyα, transition. This results in a the Lyα absorption line at 1216 Å in the rest frame of the absorber. The actual observed line, λ_{obs}, will have been shifted according to the redshift of the absorber, $\lambda_{obs} = (1 + z_{abs})1216$ Å. In quasar spectra the Lyα absorption is always found bluewards of the quasar Lyα emission line since $z_{abs} < z_{qso}$.

The strength of the absorption lines are of course dependent on the amount of neutral hydrogen along the line-of-sight, the column density of neutral hydrogen, N_{HI}. N_{HI} is a useful physical quantity for the absorbers and is used to divide the Lyα absorbers into several groups. Mainly the Lyα forest, Lyman limit system, LLS and the highest N_{HI} absorbers, the damped Lyman-α absorbers/systems, DLAs.

The most common Lyα are the numerous HI absorbers with $10^{12} cm^{-2} \leq N_{HI} \leq 10^{17}\, cm^{-2}$, which are the components of the Lyα forest. However, the Lyα forest is actually highly ionized and do only have a HI fraction of $\sim 10^{-11}$(Longair 2008). These absorbers are expected to be situated in the intergalactic medium. The Lyα forest dominates in the quasar spectra for $z_{qso} \gtrsim 6$ when the absorbers become so dense that for some spectra all the light is absorbed. This is called the Gunn-Petersen through(Longair 2008).

1.1 Lyman Limit Systems, LLS

Lyman limit systems, LLS, are absorbers for which the neutral hydrogen absorb all the photons with a higher energy than 13.60 eV. The photons are absorbed since they all have a sufficient energy to ionized neutral hydrogen. This energy corresponds to all wavelengths below $912(1+z_{abs})$ Åand is refered to as the Lyman limit. The resultant feature in a spectrum is seen as a sudden drop of

flux going from higher wavelengths to lower, see e.g. figure 1. The feature is called a Lyman break if the neutral hydrogen absorb ALL the quasar photons below the limit, and a partial Lyman break if it is only a fraction of the photons which are absorbed. The N_{HI} required for a Lyman break is $N_{HI} > 10^{17} cm^{-2}$ and is thus the lower limit for LLS.
The Lyman break is also observed in high redshift galaxies, Lyman break galaxies. Special methods to detect this break has been used to find high redshift galaxies.
The highest column density hydrogen absorbers are the Damped Lyα systems, DLAs, with $N_{HI} \geq 2 \cdot 10^{20}\, cm^{-2}$. DLAs are in principle LLS, however, they do have very different properties. Due to the high N_{HI} they show damped profile wings, along with the very broad feature, it makes DLAs very recognizable in quasar spectra. The high N_{HI} also means that DLAs are the absorbers with the largest neutral gas content, and DLAs are therefore important reservoirs of HI in the universe. In dex the DLA threshold is $N(HI) > 20.3$. There is also a sub group of DLAs which show the same damped wings feature, however, they do have other properties, which will be further outlined. The sub-DLAs have $10^{19} \leq N_{HI} \leq 2 \cdot 10^{20}\, cm^{-2}$.

2 DLAs - Damped Lyman-α Systems

The DLA threshold is $N_{HI} > 2 \cdot 10^{22} cm^{-2}$,

2.1 Self-shielding

The special property which separates DLAs from the other Lyα absorbers are the fact that DLA gas is mainly neutral. By measuring the HI of DLAs through the 21-cm line the spin temperature has been observed to be below 1000 K, and shows the gas to be cold and quiescent(Wolfe, Gawiser & Prochaska 2005). The cold neutral gas for DLAs is due to self-shielding. The high column densities has the effect that most of the UV-light is absorbed in the outer parts of the cloud and the inner part is therefore protected. This result in a higher percentage of the hydrogen being in neutral form than e.g. sub-DLAs. The photons with energy lower than the Lyman limit will, however, be able to penetrate into the cloud. These photons can ionize metals to single ionization states, but not any further since the cloud is shielded from this. Very high energy photons will also enter the cloud and ionize metals to single and doubly ionized species. However, high energy photons do have very low interaction cross-sections and it is relatively little ionization they cause. Thus there are not many ionization lines which need to be accounted for and ionization corrections are normally not necessary for DLAs. The main ionization lines are observable when redshifted into the wavelength range of ground based telescopes. This means that it becomes relatively easy to estimate DLA metallicity. The typical metallicity and N_{HI} estimates give errors of 0.1 dex(Wolfe, Gawiser & Prochaska 2005).

2.2 Damped wings and curve of growth

DLAs (and sub-DLAs) do not only have the physical condition of high neutral content, but the Lyα line do also appear different than for other Lyα absorbers. This is also due to the high N_{HI}. Spectral linestrengths and shape are a mixture of several line profiles because the particles which are producing the line, may it be an absorption or emission line, is influenced by several physical factors. The main factors shaping the line is the Doppler effect and the natural broadening. The natural broadening is due to the fact that energy states are not infinitely sharp and do by nature have a propability of deviating from the central value. The energy range ΔE are estimated from the uncertainty principle, $\Delta E \Delta t \geq \hbar/2$, and the finite lifetime, Δt, of the decaying excited state, The two effects are forming line shapes best described by the two line profiles, the Gaussian and Lorentzian profile. Where the Gaussian is for the broadening due to the doppler effect and the Lorentzian is more suitable for describing the natural broadening. The two profiles fall differently off from the centre of the line, λ_0, since they are proportional to(Wolfe, Gawiser & Prochaska 2005):

$$\text{Gaussian Profile} \propto \exp\left(-\frac{|\lambda - \lambda_0|^2}{\lambda_0}\right) \quad , \quad \text{Lorentzian Profile} \propto \frac{1}{|\lambda - \lambda_0|^2} \tag{1}$$

From equation 1 one see that near the centre the Gaussian profile is dominating and further out it is the Lorentzian function, since the exponential will decrease at a higher rate than the inverse square. Therefore there are different regimes where the two effects are dominating.

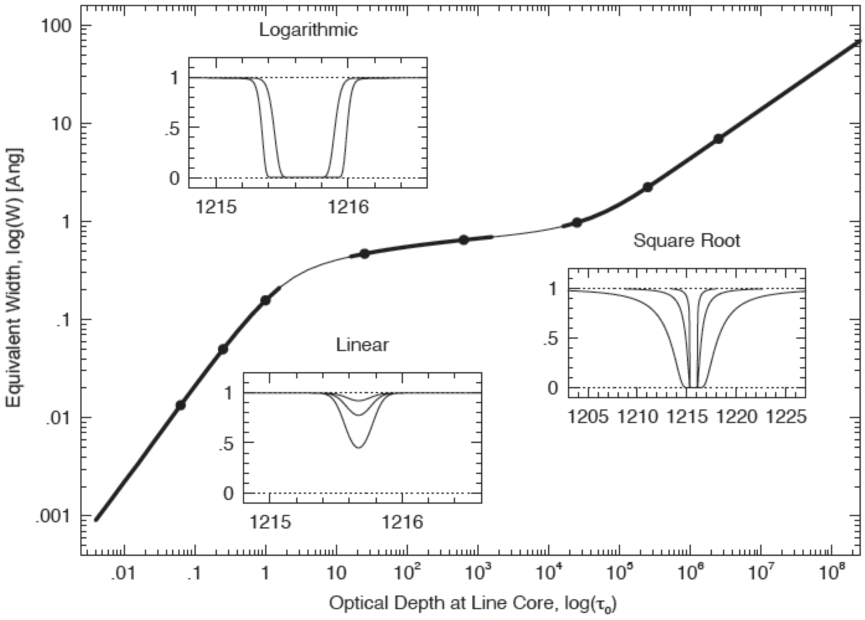

Figure 2: http://www.ast.cam.ac.uk/~pettini/Physical%20Cosmology/lecture10.pdf

One of the parameters determining how weak or strong a line appears is the column density, N_{HI}. How a line grows is dependent on how strong it is. A curve of growth illustrates how the equivalent widht(see Appendix A) ,EW , increases as a function of N_{HI}, see figure 2. The growth of a spectral line is divided into three different regimes, the linear, flat(logarithmic) and damped(square root). Considering a weak Lyα absorption line which is present due to a low N_{HI} medium where N_{HI} keep increasing(see figure 2). The EW grows linearly with the column density for this weak line. But as the line eventually saturates the EW almost stop growing. The saturated line, if resolved, is seen as total absorption, and has an rectangular shape. However, the wings of the line do keep expanding and will eventually become visible again. The EW now grows mainly due to the wings, not as effective as in the weak/linear domain, but as $EW \propto \sqrt{N_{HI}}$.

2.3 Voigt profile

As mentioned a line profile is a combination of thermal doppler broadening and natural broadening, which is represented by the Gaussian and Lorentzian profile respectively. The optimal line profile describing a normal spectral line is the Voigt profile, which is the combination of the two profiles. The Voigt function does not have a simply analytical version but can be approximated. For this thesis the following version of the Voigt function is applied to fit DLAs in order to obtainN_{HI}(García 2006):

$$F(x) = \exp\left(\frac{4\sqrt{\pi}e^2}{bm_e c} f\lambda_0 N_{HI} H(a,x)\right) \tag{2}$$

$H(a, x)$ is the Voigt-Hjerting function and this is the part which is approximated for the purpose of fitting the DLAs. The constants in equation 2 are the base of the natural logarithm, e, the speed of light in vacuum, c, and the mass of the electron, m_e. The other parameters are the doppler parameter, b, the oscillator strength, f, and the wavelength of the transition, λ_0. The variable x is a function of the wavelength, $x = \frac{\lambda-\lambda_0}{\lambda_0}\frac{c}{b}$. For the Ly$\alpha$ transition $f = 0.416$. The zeroth and first order of the $H(a, x)$ function is necessary for high N_{HI} absorbers. The zeroth order is $H_0 = e^{-x^2}$. For the Lyα transition $\Gamma = 6.265E8$. The first order term of $H(a, x)$(García 2006):

$$H_1(a,x) = -\frac{a}{x^2\sqrt{\pi}}\left(H_0^2 \cdot \left(4x^4 + 7x^2 + 4 + \frac{3}{2}x^2\right) - \frac{3}{2}x^2 - 1\right) \tag{3}$$

Here a is the damping parameter and is defined as $a = \frac{\lambda_0\Gamma}{4\pi b}$, which include the damping constant Γ. Equation 2 with the approximation $H(a, x) \approx (H_0 + a \cdot H_1)$ is the function applied in the fitting of DLAs to determine the N_{HI}.

2.3.1 b-parameter

The b parameter is the doppler width, the most probable speed along the line of sight. The velocity of the gas is a combination of the temperature and macroscopic motions of the gas. For DLA Lymanα lines b ranges from $10 - 100\,km/s$ and the median value is $b_m = 36\,km/s$(García 2006). For the most DLAs these values of doppler width have no or very little effect on the line profile. As explained in section 2.2 for high $N_{HI}(> 10^{19}cm^{-2})$ the line will be in the domain where the damped wings are dominating the profile. The wings are caused by the natural broadening and not the doppler broadening. Thus the Voigt profile is for most DLAs independent of b which then can be set to a constant.

2.4 Proximate DLAs

Proximate DLAs have the Ly$-\alpha$ line very close to the quasar. The definition of the distance is given in the relative velocity, δv, which is set to $3000\,km/s$ for the limit of proximate DLAs. δv can be calculated from the redshift of the quasar and the dla redshifts, z_{em} and z_{abs} (Ellison et. al 2010):

$$R \equiv \frac{1+z_{abs}}{1+z_{em}} \qquad \delta v = c\frac{R^2-1}{R^2+1} \tag{4}$$

The proximate DLAs are assumed to be connected with the quasar enviroment. The properties of these DLAs are therefore possible quite different from other DLAs, for example the ionization level might be higher since it is near this high energy source(Ellison et. al 2010).

2.5 Quasar as background source

Quasars are the most luminous active galactic nuclei, situated in the centre of massive galaxies. The high radiation originates from accretion onto a super massive black hole. The most of the energy from quasars is in UV and the optical regime but do in fact cover most of the electromagnetic spectrum. As the neutral gas is mostly absorbing due to photoionization, the absorption lines from neutral clouds are in the optical as well. Therefore quasars are optimal to study the intervening gas. The optical quasar spectrum is believed to originate from the accretion disk near the super massive black hole. This spectrum is a combination of several black body spectra which result in a power law continuum. However, there are also many very broad emission lines. Optical quasar spectra do vary from one another other. The line strength of the emission lines can vary lot and over time as well. Some of the lines also show a tendency of being blueshifted. Thus it is not trivial to predict the spectrum of a quasar before it being absorbed by intervening clouds. Especially at high redshift where the number of absorbers are higher and not only the Lyα lines but also Lyβ and the metal absorption lines are present in the spectrum. The broad DLAs are also able to completely 'wash' out the profile of the broad quasar emission lines. Thus it is an advantage to assume an average spectrum. In this thesis the quasar composite spectrum compared with the data is Telfer et al. 2001. It is constructed from a sample of 184 quasar spectra with $z > 0.33$ observed with the Hubble Space Telescope. This quasar composite template is further discussed in regards to the analysis of the spectra in section 16.2.

2.6 Searches for DLAs

There is of course limits for which redshift DLAs are observable. The upper limit is due to the noise from the Lyα forest. For $z > 5.5$ the Lyα forest is so dense that essentially no DLA will be significantly observable(Wolfe, Gawiser & Prochaska). There is essentially no lower limit for where a DLA can be observed. However, it is very unlikely to observe DLAs in the local universe because of the low cross-section. There are also the obstacle of DLAs with $z < 1.65$ since then the Lyα line is in the UV. This is of course obtainable to gain a UV spectra with space telescopes. For high redshift quasars there is a problem due to the fact that a Lyman break is likely to be at higher wavelength than the DLA, since Lyman limit systems are much more common than DLA systems.

Since all rest frame equivalent widths of Mg II lines in DLAs are quite large, there has been searched for absorbers with this criteria in order to identify new DLAs. An example is Rao et al. 2006, where quasar spectra in The Sloan Digital Sky Survey, SDSS , was searched for absorbers with the requirement of a high EW of the Mg II line $\lambda 2796$($EW_0 > 0.3$ Å). The quasars was afterwards observed in the UV to confirm if they were DLAs or not. This showed to be a great method to find new DLAs with $30 - 40\%$ of the observed quasar spectra showing detections.
This same method has also been applied for large EW doublet Ca II $\lambda 3934$,$\lambda 3969$ for even lower

redshifts(König et al. 2006). If a quasar sight line is near a galaxy which could be responsible for a Ca II absorption in the quasar spectra it is a good candidate galaxy counterpart.

Large surveys, such as The Sloan Digital Sky Survey has systematically and automatically been searched for DLAs. This requires criteria, one of them of course being a high EW for the absorption. These systematic searches do have some biases, which will be explained further in section 5.

3 The distribution of N_{HI}

The number distribution of N_{HI} is a product of the cross-section of the absorber times the comoving number density. The overall distribution of N_{HI} is mainly statistical. It reflects the possibility of hitting an extended cloud with some declining HI gradient from the centre. Due to the different probabilities of the impact parameter of such an object it is more likely to measure a low N_{HI} than a high N_{HI}(Longair 2008). The HI frequency distribution $f(N,X)$ is well described with both a double-power law function and a Γ function, which is a power-law with an exponential turn-over, see figure 3. A single power law is not applicable since a steeper decrease of $f(N,X)$ is seen for high N_{HI}. For the double power law the break column density is in the high end of the DLA N_{HI}. The shape of $f(N,X)$ is approximately the same for all redshift ranges, however, the scaling of the function do decrease for lower redshifts. However, it has also been shown that it flattens at lower redshift for the low N_{HI} end of sub-DLAs(Zafar et al. 2013). This implies fewer sub-DLAs in at low redshift.

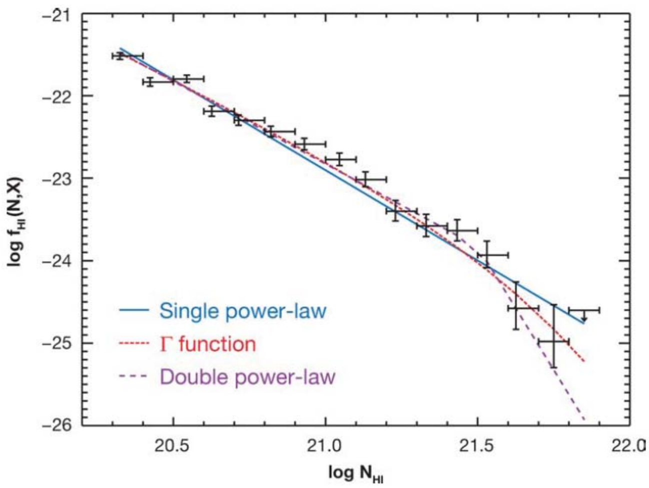

Figure 3: Prochaska, Hert-Fort & Wolfe 2005: figure 6. This is the for the HI frequency distribution, at redshift 3. The data is from SDSS data release 3.

4 DLAs and galaxies

The neutral hydrogen column densities, N_{HI}, for DLAs are comparable to the N_{HI} for sight-lines through the Milky way disk. Therefore the DLAs are possibly similar to interstellar media for other galaxies. While sub-DLAs with lower N_{HI} is similar to sight-lines through galaxy haloes and are thus more associated with these.

Galaxies and DLAs have been shown to be connected in several ways, and the a theory is that they at high redshifts were small proto galaxies which eventually merge and a evolve into the galaxies we see in the nearby Universe. This has been shown with models(Haehnelt et al. 1998) which is consistent with the velocities observed in DLAs. This is probably a regular process where the DLAs contribute to the star formation. The N_{HI} threshold is actually also consistent with being the lower limit for which star formation is occuring in nearby spiral galaxies(Kennicutt 1998). However, DLAs have also been observed in connecting with massive metalrich galaxies(e.g. Fynbo et al. 2013). In fact the types of galaxies which have been confirmed as DLA absorbers are both dwarf and disk galaxies(Chen 2005). A clear picture of the nature of DLAs is thus not seen.

Based on local HI measured through the 21-cm line, the expected counterpart galaxies have a median gas mass of $2 \cdot 10^9 M_\odot$ and 87 % of them are low luminosity galaxies(Zwaan et al. 2005). However, the searches for DLAs are biased towards finding the higher luminosity galaxies. There has also been observed HI clouds in the nearby Universe outside galaxies which would appear as DLAs if there was a background quasar(Tripp & Bowen 2005). Since there are no information on the metals when only observing the 21-cm line, it is not possible to tell where the clouds originates from. It could possibly be clouds which was once apart of galaxies, or it could be small dark matter haloes containing gas which is not dense enough to form stars(Tripp & Bowen 2005).

5 The cosmological mass density of neutral gas in DLAs

The cosmological mass density of neutral gas in DLAs, Ω_g^{DLA}, is a measure of the total mass for systems with $N_{HI} > 2 \cdot 10^20 cm^{-2}$. Since DLAs are the largest reservoirs of neutral gas in the Universe this parameter is an important measure. The evolution Ω_g^{DLA} is especially and will be further explained from previous studies in this section. But first the calculations necessary to deduce the cosmological mass density of neutral gas, Ω_g^{DLA}, are presented, along with possible biases when calculating Ω_g^{DLA}. In order to tell about a cosmological parameter from a relatively small sample one has to use statistics. The column densities of the gas in the DLAs need to be scaled according to how many absorbers it is possible to detect. The possibility of detection is proportional to how many quasars spectra was searched and the ability to detect DLAs in the spectra. Given a lower and higher redshift limit, z_{min} and z_{max}, of a possible detection of an absorber the total path length is found from:

$$\Delta X_i = \int_{z_{min}}^{z_{max}} \frac{(1+z)^2}{\sqrt{(1+z^3)\Omega_m - (1-z)^2(\Omega_m + \Omega_\Lambda - 1) + \Omega_\Lambda}} dz \tag{5}$$

ΔX_i is for one spectrum, all the values for the spectra in the sample need to be summed to give the final total path length, ΔX. Ω_g^{DLA} is essentially the sum of all the measured column densities of neutral hydrogen $N_{tot} = \Sigma N_{HI}$ for the DLAs, $N_{HI}(\geq 2 \cdot 10^{20}\, cm^{-2}$, normalized to the current critical mass density ρ_c (see Appendix B) and ΔX (e.g. Wolfe, Gawiser & Prochaska 2005):

$$\Omega_g^{DLA} = \frac{\mu m_H H_0}{c \rho_c} \frac{N_{tot}}{\Delta X} \tag{6}$$

The gas consist primarily of hydrogen, however, to account for the non-negligible fraction of helium as well the mean molecular mass, μ, of the gas along with the mass of the hydrogen atom m_H is included in equation 6. For a fully neutral gas $\mu = 1.3$ with a composition of 75 % hydrogen and 25 % helium.
Ω_g^{DLA} can also be determined by integrating $f_{HI}(N, z)$ instead of the sum in equation 6. This should work well for a large sample of absorbers where $f_{HI}(N, z)$ can be significantly determined(e.g. Zafar et. al 2013).

5.1 Bias effects

Bias effects are very important to consider when calculating Ω_g^{DLA}, many of which can be avoided by choosing a proper redshift interval for ΔX. The edge effect(Noterdaeme et al. 2009) is one if such biases. The edge effect is due to lower S/N for the blue end of the spectrum. If a high N_{HI} DLA is present in this low S/N it lowers the signal and S/N even further. This will possibly affect the determination of the systematically determined z_{min} for the spectrum, since z_{min} previously was determined by a criteria of a certain level of S/N. This will result in the presence of a DLA actually not being identified. This effect is especially valid for the lower redshift DLAs, since they of course are closer to the 'edge' of the spectrum. By not correcting this the result will be a lower Ω_g^{DLA}, since a fraction of high N_{HI} DLAs might be missed. A method to correct this is to shift all systematically determined z_{min} redwards in the spectrum. The wings of DLAs, especially for high N_{HI}, are really broad, and to avoid them a velocity shift of $10,000\, km/s$ has been found necesarry(Noterdaeme et al. 2009).
Another bias in systematic searched are broad absorption lines in the quasar spectra(not intervening absorbers). Especially for O IV near Lyβ and C IV can have broad absorption, which can lead to false detection of DLAs.
It has also been shown that very high N_{HI} in a sample are the DLAs which contributes the most to Ω_g^{DLA}. Even a single DLA with $N_{HI} = 10^{22} cm^{-2}$ in the sample makes a large difference to the determination of Ω_g^{DLA} (Noterdaeme et al. 2009). However, a more recent study show that systems with $N_{HI} > 5 \cdot 10^{21} cm^{-2}$ only contribute with 10 % to the total Ω_g^{DLA}, but it still is DLAs with $N_{HI} > 10^{21} cm^{-2}$ which contributes the most(Noterdaeme et al. 2012)

At high redshift($z > 4$) the Lyman-α forest becomes really dense. Therefore it is difficult to fit the DLA profiles. It is still possible but it might result in an overestimation of N_{HI}.

As explained in section 2.4 proximate DLAs are possibly not as large neutral gas reservoirs compared to their N_{HI} and is in general not included in estimations of Ω_g^{DLA}(Ellison et. al 2010). Including proximate DLAs will most likely result in an overestimation of Ω_g^{DLA}.

5.2 Previous studies

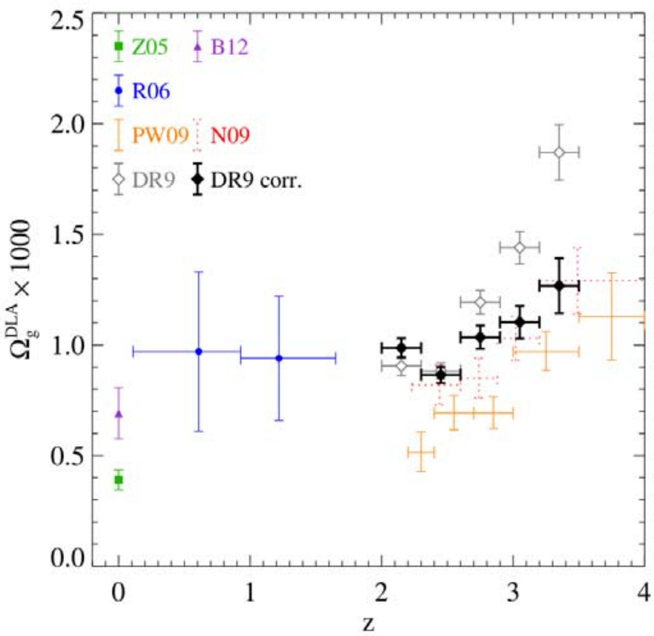

Figure 4: Noterdaeme et al. 2012: figure 3. The black bins are for the data for Noterdaeme et al. 2012, DR9, the grey bins are the uncorrected data. The red dashed bins are for data from a previous SDSS release, DR7, Noterdaeme et al. 2009, N09. The orange bins are for Prochaska & Wolfe 2009, PW9. which is for SDSS data release 5. The blue bins are from Rao et al. 2006. The purple bin is for Braun 2012, B12, and the green for Zwaan. et al. 2005, Z05.

Figure 4 shows previous Ω_g^{DLA} obtained from several different data. The local($z = 0$) Ω_g^{DLA} values are from the detection of the 21-cm emission line of neutral hydrogen. Ω_g^{DLA} is calculated from the integral mass of HI measured in galaxies. The lowest point in figure 4 is from Zwaan et. al 2005, and is calculated from a sample of 355 HI maps. This study shows that the DLAs contribute to $\approx 81\%$ of Ω_g^{DLA} and the remaining contributor is high N_{HI} sub-dlas. The higher local Ω_g^{DLA} point is from Braun 2012, where there has been corrected for the opacity of the line. This sample only contains three galaxies.
The Rao 2006 et al. sample contains 41 intermediate redshift DLAs, $0.11 < z < 1.65$. However, they all have large equivalent widths of Mg II lines, and possible therefore biased. Since it was chosen to be DLAs with a specific property it might be biased.
The high redshift Ω_g^{DLA} values are from different systematic studies of large DLA samples, mainly from SDSS. For N09 and PW09 the edge effect has been avoided. The plot is from Noterdaeme 2012. Their method to avoid biases is as follows. Given the bias mentioned in this section, the highest probability of identifying the absorbers are between the Lyα and Lyβ quasar emission lines. This way one avoids the broad absorption features and the edge effect in systematic searches. More specifically the region between 3000 km/s redwards of the Ly-β emission line and 5000 km/s bluewards of the Ly-α emission line was applied to calculate ΔX. Only quasars with $z = 2-3.5$ was selected, to avoid the very blue end of the spectrum. Besides this there was also corrected for other systematics, incompleteness of the sample and over or under estimates of N_{HI} measures. There are some differences in the observations, but Noterdaeme et al. 2012 argue that the difference from PW9 and DR9 are due to the fact that DR9 has a larger contribution from high N_{HI}. The overall evolution of Ω_g^{DLA} do seem as if it is constant until a redshift of ~ 0.5(Rao et al. 2006) where it begins to be more or less decreasing, dependent on which of the two local measurements is the most probable.

It is mainly DLAs which contribute to the total mass density of neutral gas, Ω_g, however there is of course also a contribution from other Lyα absorbers. The sub-DLAs has been shown to contribute with 8-20 % of the total Ω_g(Zafar et al. 2013).

Several factors play into the evolution of Ω_g^{DLA}. The main effect of Ω_g^{DLA} is assumed to be that the neutral gas will contribute to the formation of stars. An evidence for this theory is for example seen via the star formation density/history, which seems to follow the same trend as Ω_g^{DLA}(Hopkins et al. 2008). However, the similar mass density parameter for visible stars, Ω_*, is in the local universe 2-3 times lower than at high redshift(Wolfe, Gawiser & Prochaska 2005). Therefore the star forming gas must be replenished with new neutral gas. Meaning that some recombination of ionized gas is needed(Zafar et al. 2013).

6 Metallicity of DLAs

DLAs do in general have low metallicities. In a recent study a mean metallicity of [M/H]=-1.51 was estimated from 207 DLAs with $z > 1.5$(Rafelski et al. 2012). For lower redshifts the data is biased by the fact that the DLAs are often found from high metallicity lines. For local DLAs the mean metallicity has been estimated to be [O/H]=-0.85 ± 0.2(Zwaan et al 2005).

Even though DLAs in general do have low metallicities, a category of DLAs with strong metal lines are observed(e.g. Kaplan et. al 2010). These are called metal strong DLAs, MSDLAs, and have median metallicities in the order of [M/H]~ -0.7(Kaplan et al. 2010). Even DLAs with solar metallicities have been observed(e.g. Fynbo et al. 2011).

A metallicity floor for DLAs is also observed at $[M/H] = -3$. This limit might be present if the metallicities follow a Gaussian distribution since the probability of finding a DLA in the low end wing will be extremely small(Rafelski et al 2012). Physical explanations has also been proposed, e.g. a pre-enrichment by Population III stars(Wise et al. 2012).

The metallicity do in general show a great scatter for all N_{HI} and there do not seem to be any correlation between the two(Rafelski et al. 2012). This possibly reflects the various masses of the DLAs. The mass-metallicity relation of galaxies is explained from the fact that more massive galaxies have a large gravitational potential. The large gravitational potential makes the galaxy efficient at holding on to the neutral gas and metals. A large gas mass will increase the star formation and thus the metallicity as well.

The metallicity scatter is shown for all redshifts out to a redshift ~ 5. The scatter of metallicities as a function of redshift is ~ 0.5 dex(Rafelski et al. 2012). One might expect an increase in metallicites with decreasing redshift, since the ongoing star formation in galaxies will keep enriching the Universe with metals. However, it might not be as simple, since DLAs in principle do not have to follow this Universal trend. But a decreasing trend for the mean metallicities with increasing redshift is actually measured. It follows a linear trend with a slope of -0.22 ± 0.03 dex per unit redshift(Rafelski et al. 2012).

The distribution of metallicities for DLAs with $2 < z < 5$ are actually comparable to the distribution for halo stars(Rafelski et al. 2012). More precisely the fraction of α elements to iron, [α/Fe], for halo stars and DLAs can be drawn from the same parent population(Rafelski et al 2012). The ratio [α/ Fe] is a tracer of star formation rate. This is because Fe is mainly released into the ISM by Type Ia supernovae and α elements in Type II supernovae. Due to the nature of these super novae types there is a time lag of $\sim$1 Gyr for Fe relative to α elements(Pettini & Pagel 2004). Both halo stars and DLAs have enhanced α elements of [α/ Fe]≈ 0.3, this show that halo stars might have formed out of DLA gas(Rafelski et al 2012).

DLAs and sub-DLAs are measured to have the same metallicity distribution for $z > 1.7$. There has been observed a higher metallicity for sub-DLAs for lower redshifts($z < 1.7$)(Dessauges-Zavadsky et. al 2009). However, this is likely a selection effect, since the low redshift sub-DLAs was found from the requirement of a large Mg II equivalent width.

7 Measuring metallicities of DLAs

As mentioned in section 2.1 it is relatively easy to measure the metallicity of DLAs since they are mainly neutral. The metallicities are found from the column density of the heavy elements. A method to obtaining the column densities is e.g. via the apparent optical depth method, see Appendix C. The elements which give the most precise metallicity measure are O, S, Si, Zn and Fe. However, oxygen is for most DLAs unobservable and some elements, especially Fe, do require a measure of dust depletion.

7.1 Equivalent width of SiII 1526

There is expected to be a relation between kinematics and the metallicity in DLAs. Followed by the mass-metallicity relation, and the fact that the velocity is proportional to the mass of the system, a higher velocity dispersion for measured metal lines might indicate a higher metallicity.

The width of a resolved line can be converted into a velocity width.(e.g. Møeller et al. 2013) Since metal lines in DLAs are often composed of several small absorbing 'clouds' the equivalent with, EW, is a useful property for investigating the line kinematics. A well established empirical relation is between the metallicity, $[M/H]$, and the rest frame equivalent width of Si II 1526, EW_{1526}. It is in fact the tightest correlation between the metallicity and another DLA property(Prochaska et al. 2008):

$$[\mathrm{M/H}] = (0.92 \pm 0.05) + (1.41 \pm 0.10) \log(EW_{1526}/1\text{Å}) \tag{7}$$

The relation is a power law and the calibrated data has a scatter of $1\sigma = 0.25$ dex and are all DLAs with $z > 1.6$, see figure 5. The DLAs were selected to have high N_{HI}. When EW_{1526} is higher than 0.3 the line profile is highly saturated and do not necessarily reflect the gas metallicity. However, it has been observed that the relation do in fact extend out to even solar metallicities(Kaplan et al. 2010).
Prochaska et al. 2008 also find some kind of correlation between EW_{1526} and N_{HI}, see figure 6. There are no absorbers which show a low EW_{1526} and high N_{HI} values. When EW_{1526} is higher than 0.3 there is a larger scatter of the measurements. There is not a physical explanation for a relation between the metallicity and N_{HI}. One might assume this since there is the mass-metallicity relation for galaxies(Tremonti et al. 2004). However, the DLA column density are more dependent on the impact parameter for the intervening absorbing clouds than the actual total amount of gas. N_{HI} is in general therefore not by itself a measure of mass.

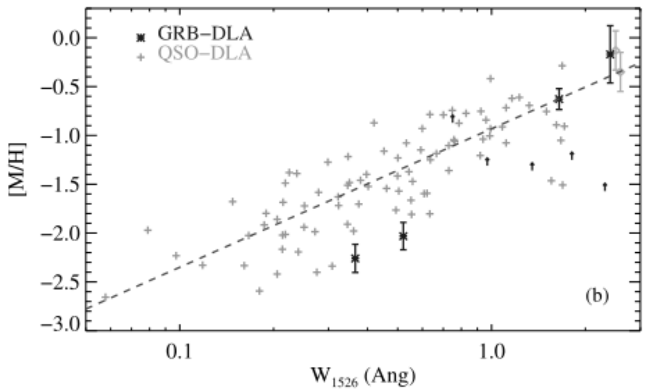

Figure 5: Prochaska et al. 2008: Figure 6. The correlation between the equivalent width of SiII 1526 and the metallicity is shown here here. There are both points for QSO- and GRB-DLAs. The GRB-DLAs do not seem to follow the same trend as the QSO-DLAs. The dashed line was only fitted to the QSO-DLAs.

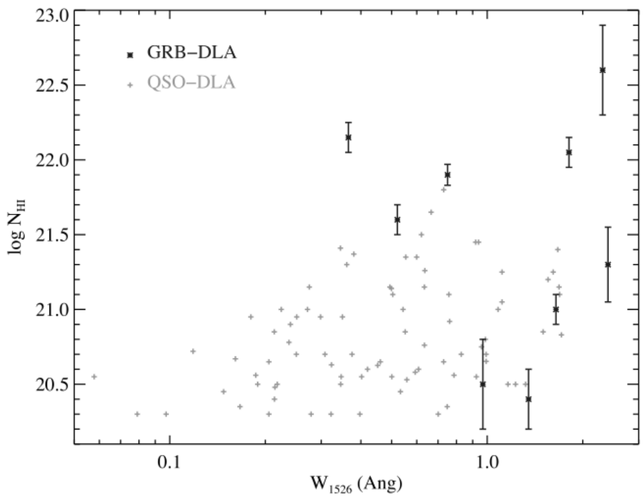

Figure 6: Prochaska et al. 2008: Figure 7: Here is DLA column densities plotted as a function of the equivalent width of SiII 1526.

8 High redshift DLAs in the X-shooter Large Programme

In the beginning of 2014 we have completed a large VLT/X-shooter[1] programme (Principle investigators are Sebastian Lopez (Chile), Sara Ellison (Canada) and Valentina D'Odorico (Italy)), which consists of X-shooter spectra of 100 quasars at $z > 3.5$ with a high S/N ratio over the entire wavelength range. Only 85 of the 100 quasars are analysed in this thesis since the remaining 15 was not processed in proper time to be included.
The redshifts for possible DLAs in the X-shooter sample is of course dependent of where the quasar Lyman α line might be in the spectrum. The lowest observable wavelength for X-shooter is 3000 Å. This limit correspond to a DLA $z = 1.63$. This lower limit is most likely too low, since, as mentioned in section 2.6, there will likely be a Lyman (partial) break which absorbs most of the quasar light for higher wavelengths. Especially since these are quite high z quasars, see figure 7.

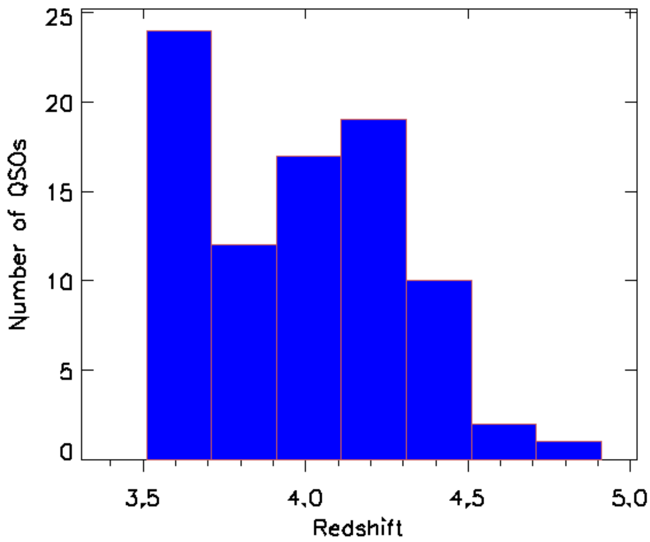

Figure 7: The redshift distribution of the 85 X-shooter quasar sample analysed in this thesis.

The highest redshift DLAs observable in the sample is of course giving by the highest redshift quasar observed. The highest redshift for one of the quasars is $z = 4.72$(BR J0307-4945), meaning the Lyman α line of this is at ~6950 Å. The lowest redshift quasars observed has $z = 3.51$([HB89] 1159+123 and SDSS J133254.51+005250.6). The majority of the quasars have redshifts $z_{qso} \approx 3.5 - 4.5$. The DLA redshifts are expected to have the highest possibility of detection for redshifts not much lower than the sample z_{qso} (see section 5). Therefore the range for the quasar redshifts are most likely $z_{dla} = 3 - 4$.

9 Disk galaxies

9.1 Spectra

A galaxy emits over a large range of wavelengths. The contribution to the spectra of galaxies are of course the constituents of the galaxy, the stars, gas and dust.
The main emitting part in a starforming galaxy is the HII regions. These are ionized gas clouds, also called nebulas. The power of the optical light of a galaxy decreases with distance, d, approximately as d^{-2}(Sparke & Gallagher 2006). The gas is heated and ionized by photons from O and B stars. A fraction of the UV photons is absorbed by dust and re-radiated in the infrared. The ionized gas show emission lines due to recombination of hydrogen atoms. There are also regions with recombination lines from ionized helium near the O stars(Emerson, D. 1996). Most other atoms are producing emission at the specific transitions after collisions with electrons. Because of the low density in nebulas even forbidden transitions are possible. Forbidden transition lines are denoted with square brackets, e.g. [N II](Emerson, D. 1996)
The neutral gas, HI, is possible to observe via the 21-cm line transition in the Milky Way and nearby galaxies. The power of this line decreases with radial distance in the same manner as the power of the optical light(d^{-2}). However, the gas exceeds the distance of the optical emitting part of galaxies with about twice as much. 10-20 % of galaxies have been observed to have

[1] X-shooter: Vernet et al. 2011, A&A, 536A, 105 at the, VLT, Very Large Telescope

neutral gas beyond 2 R_{25}. R_{25} is defined as the 25 magnitude $arcsec^{-2}$ B-band isophote(Sparke & Gallagher).
The column density of HI in spiral galaxies is approximately the same regardless of it being a normal star forming or a low-surface brigtness galaxy. The neutral gas in disk galaxies has the highest concentration in the disk, and a further high concentration in the spiral arms. However, HI can reach several kpc above the plane of the disk, probably due to star formation feedback, e.g. super novae and galactic winds.

9.2 Velocity gradients

If one uses the emission lines in the HII region to measure the velocity, the velocity gradient will mainly be due to the stars in the galaxy(Mundell & Shone 1997). The stars will follow the overall motion of the galaxy determined by the gravitation potential. This is mainly dominated by the dark matter which is present out to far beyond the visible matter in the disk. The velocity gradient from the stars do thus flatten out after a certain distance from the centre of the galaxy. Another method of measuring the velocity gradient is using the hydrogen 21-cm line. The 21 cm line has in fact been used to map velocities in nearby galaxies. Through the neutral hydrogen line it is the gas movement in the galaxy which is mapped. Thus this will show sign of e.g. galaxy winds and shocks in the ISM.

9.3 Balmer decrement

A simple way to estimate the reddening from dust in galaxies is from the ratio of the Balmer lines. The ratio of the lines is theoretically determined(or measured?) to be specific values for certain temperatures and electron densities, n_e. The Balmer lines with the largest line strengths are of course Hα and Hβ. The intrinsic ratio Hα/Hβ is determined to be 2.87 for 10.000 K and 2.67 for 20.000 K(Emerson, D. 1996) with $n_e = 10^2\, cm^{-3}$. Since it does not show a large dependency on the temperature it is fair to assume the 10.000 K scenario(case B) in general for normal star forming regions. Another well determined Balmer line is Hγ and this might also be compared to Hα and/or Hβ. The way of estimating the dust reddening is thus to assume that any deviations from the theoretical value is due to dust extinction. This is because dust will absorb more of the blue part of the spectrum than the red, meaning the Hβ and Hγ lines will be more extinguished than Hα.

Though there are other contributions/effects one might need to take into account, etc. the ionization mechanism/environment. In AGNs the intrinsic ratio is larger since Hα is increased due to collisions of particles in partly neutral gas(Emerson, D. 1996). If this effect is not taking into account the dust reddening will appear larger than the true reddening.

10 Measuring metallicities of galaxies

As described in section 6 metal lines might be represented as absorption in the spectrum, for e.g. DLAs in QSO spectra. But for galaxies which are emitting, the way of measuring the metallicity is via emission lines in the HII regions. The most clear lines are in principle from the most abundant metals, and these are thus prefered for line diagnostics. Some of the strongest optical metal lines emitted in HII regions are [N II], [O II], [O III], [S II] and [S III].

A 'direct' method of measuring the abundance is calculating the electron temperature from line ratios of auroral to nebular lines, the T_e method(Osterbrock 1989). A line ratio might e.g. be [O III] $\lambda 4363/\lambda 5007$, however, the auroral line $\lambda 4363$ becomes fainter with increasing metallicity. Therefore this method easily becomes difficult to obtain the metallicity from. However the strong nebular lines still remains and might be used to infer the metallicity via other methods. The strongest emission lines are also applied in photoionization models of the HII regions. The models are also a method to obtain the metallicity for star forming galaxies(Ferland et al. 2013).

But these analysis methods include either very high resolution and/or complicated modelling, and thus in some cases it is preferred to use other simpler methods. For example cases where only a few metal lines are available. This could be for higher redshift galaxies where the weakest of the strong emission lines will not be resolved.

10.1 Simple line ratios

A simplified method of obtaining metallicities is to look at single line ratios of emission line intensities. For such a method it is useful to consider lines within a short wavelength 'distance' from one another. By choosing lines near each other in the spectrum one might avoid problems with different flux levels, e.g. due to extinction, and thus one do in principle not need to account for that. Since the extinction is approximately the same for a short wavelength interval, it will cancel out when taking the ratio of the intensities. The lines applied in this thesis are not separated with more than 150 Å at low redshift.

But the relation between line ratios and metallicity is not obvious, and do in principle not even follow a proportional relation. This is e.g. because the line strength of different elements is also highly dependent on the ionization and not just the metallicity. A lot of the elements do in fact often have many ionization transitions, which the single lines in a spectrum often represents, and thus a single line transition is also dependent on e.g. the temperature. Therefore certain line ratios show an anti-proportional relation with the metallicity, e.g. the line [O III] / Hβ. This is because a high oxygen abundance result in many excitations of fine structure levels with low energy. Decays from the fine structure levels give photons of long wavelengths, in the infra-red. The photons will escape and thus this is a very effective way of cooling the gas. [O III] transitions at 5007 Å and 4959 Å are very sensitive to the temperature and the intensity of the line will decrease with an increase of oxygen(Emerson, D. 1996)
Different very common and high strength lines have been used to find relations between line ratios and the metallicity. By measuring the metallicity via 'direct' methods(e.g. the T_e method) and plotting this metallicity as a function of the line ratios, it can be shown if there is in fact a correlation between them. Some of the most established line ratios are including the Balmer lines, Hα and Hβ, along with [N II] and [O III] (Pettini & Pagel 2004).
The most simple applied line ratio is, [N II]/Hα}, named the $N2$ index. The definition of the index is $N2 \equiv \log\{[\text{N II}]\lambda6583/\text{H}\alpha\}$. This is valid for 'metallicities', (O/H) higher than $\sim 2/5$ of the solar value. This is because the abundance of nitrogen over oxygen, (N/O), increase with (O/H) when the secondary production of N is more dominant than the primary. The primary production means nitrogen is created during the helium burning phase of stars and the secondary is when the nitrogen was already present in the medium which the stars are formed. This means that the secondary is valid latter in the evolution of a galaxy, when the interstellar gas is sufficiently metalrich. Most nearby disk galaxies do have (O/H)$> 2/5$ of the solar value and the $N2$ index is therefore applicable. The solar photosphere oxygen abundance is 12+log(O/H)$_\odot$=8.69 $\pm$ 0.05(Asplund et al. 2009). Relative to the solar abundance a measured oxygen abundance is [O/H]=log(O/H)-log(O/H)$_\odot$. The $N2$ index calibrated to measured metallicites in HII regions has given the following relation(Pettini & Pagel 2004):

$$12 + \log(\text{O/H}) = (8.9 \pm 0.04) + (0.57 \pm 0.03)N2 \tag{8}$$

$12 + \log(\text{O/H})$ is in the sense a measure of the metallicity in galaxies since oxygen is the metal which contributes with the largest metal mass fraction in the photosphere of the Sun($\sim$ 50% of the metal mass)(Rafelski et al. 2012). The data calibrated also scatter around this line with $1\sigma = 0.18$. However, there are some issues when applying equation 8 to high metallicity regions. This is because [N II] begins to saturate for lines ratios with $N2 > N2_\odot = 0.32$(Yuan et al. 2012). This means that high $N2$ are not likely to be due to high metallicities. Other causes of a high $N2$ index might be shock ionization of the gas(Yuan et al. 2012).

As mentioned the strength of [O III] is anti proportional to the overall oxygen abundance, this trend is measureable through another index, $O3N2$. The definition of the index is $O3N2 \equiv \log\{([\text{O III}]\ \lambda\ 5007)/([\text{N II}]\ \lambda\ 6583)\}$. The line ratios calibrated to metallicities give(Pettini & Pagel 2004):

$$12 + \log(\text{O/H}) = 8.73 - 0.32 \cdot \text{O3N2} \tag{9}$$

The data calibrated give a scatter around this line with $1\sigma = 0.14$. For $12 + (O/H) > 1/4 \cdot (12 + \log(\text{O/H}))_\odot$ the $O3N2$ index can be applied to deduce the metallicity to within a factor of ~ 0.25 dex(95 % confidence level). From the oxygen lines, [O III] and [O II], and Hβ a third metallicity index may be measured, the R_{23} index. However, this is a bit more complicated since it will give two values of the metallicity. This degeneracy may be corrected by using another metallicity measure which might can exclude one of the values.
It is in general a good idea use at least two metallicy indicators, since they often do not give the same result(Kewley & Ellison 2008).

11 BPT diagram

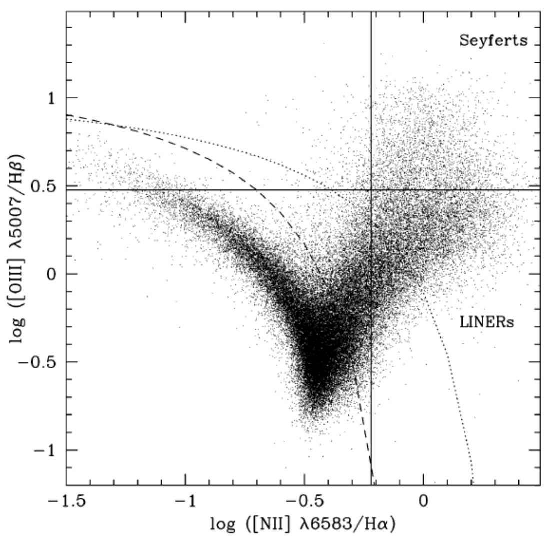

Figure 8: BPT diagram from Kauffman et al. 2003 which includes 55757 SDSS galaxies. The dashed line is indicating the separation between normal star galaxies(in the lower left region) and narrow line AGN in the two sub categories, LINERS and Seyfert galaxies.

The same line ratios as applied to calculate the $O3N2$ index is also useful at classifying galaxies. The line ratio log([O III] λ5007/ Hβ) versus the other line ratio log([N II] λ6583/ Hα) has been discovered give region of values which divide into mainly two groups of galaxies, narrow line AGN and normal starforming galaxies. This was first discovered by Baldwin, Phillips & Terlevich 1981 and this is where the diagram has its name from, the BPT diagram. An example of this is shown in figure 8 for 55757 SDSS galaxies. The dotted line is from a model(Kewley 2001), however, the data shows a clearer separation for a region with lower line ratios. For this thesis this emperical established separation line will be applied(Kauffmann et al. 2003):

$$\log([\mathrm{O\ III}]/\mathrm{H}\beta) > 0.61/\log(\mathrm{N\ II}/\mathrm{H}\alpha) - 0.05 + 1.3 \tag{10}$$

These values are of course necessary to cover the central part of the galaxy to tell if it a AGN or not. However, other parts of a galaxy can also show values in the AGN region. This can instead be a sign of shock ionazation in the galaxy.

12 Metallicity gradients of galaxies

It is highly desireable to be able to translate metallicity deduced from absorption in the quasar spectra with the absorbing galaxies. Since galaxies and quasar sight-lines not normally overlap it is important to obtain knowledge about the metallicity gradients of the galaxies.

The metalliciy gradient has of course been studied for the Milky Way. The metallicty has been measured via the HII regions and several measurements across the galaxy has shown a composite metallicity gradient of -0.06 ± 0.01 dex/kpc (Henry & Worthey 1999). In the local universe similar decreasing metallicities are observed, e.g. from Ferguson, Gallagher & Wyse 1998 a mean gradient of [O/H]=-0.09 dex/kpc was determined for disk galaxies. Some differences in the gradient is seen for the different types of galaxies. Galaxies without bars has in general steeper gradients than barred galaxies and for ellipticals it is even flatter(Henry & Worthey 1999). To measure the gradients of galaxies through the emission the galaxy of course need to be spatially resolved, and thus more gradients are determined for lower redshifts. But steeper gradients has been measured at higher redshifts. A higher resolution can e.g. be obtained with gravitational lensing. A sample of galaxies with $z = 2.0 - 2.4$ has been shown to have significantly steeper gradients > -0.2 dex/kpc(Jones et al. 2013). This sample shows that the average metallicity gradient has flattened since $z = 2.4$(last 10 Gyr) by a factor of 2.6 ± 0.9 dex/kpc(Jones et al. 2013).

12.1 Evolution

The evolution of the metallicity gradients seem to be related to merging of galaxies. It has both been shown with numerical simulations(Rupke et al. 2010a) and observations(Rupke et al. 2010b) that merging galaxies causes changes to the metallicity gradients. The numerical simulations show that merging galaxies will flatten out a possible steep metallicity gradient, and will without interactions become steeper again. While the observations of nearby interacting show that galaxies have flatter gradients than other more isolated galaxies. This is also consistent with the gradients of elliptical galaxies being observed as the flattest, since they are widely assumed to be the result of merging galaxies. A possible merger has also been observed to have a positive metallicity gradient indicating that there is occuring changes to the gradient(Jones et al. 2013). In the local universe all the measured positive gradients has also been observed in merging systems(Jones et al. 2013). Many measurements of the metallicity has been via the $N2$ index. Measurements of the metallicity with $N2$ of a AGN(Wright et al. 2004) and galaxies with outer shock regions(Westmoquette et al. 2012) has been shown to mimic positive metallicity gradients. Thus $N2$ alone cannot confirm a postive metallicity gradient.

12.2 Metallicity gradients via DLAs

The metallicity gradient can also be estimated from DLA-galaxy pairs. There are examples where the metallicity has both been found from the quasar spectrum via absorption and for the galaxy via the HII emission lines. The metallicity gradient can thus be calculated by also applying the impact parameter. For relatively high redshifts rather flat gradients has been observed as well(Krogager et al. 2013, Fynbo et. al 2013). However, these where chosen to be MSDLAs and might be biased by this fact. A recent study of 2D maps of galaxies has shown slightly steeper gradients of ~ -0.1 dex/kpc at $z \sim 1$(Péroux et al. 2013).

The gradient between a DLA and a galaxy counterpart may also be estimated indirectly. For a galaxy one can via spectral energy distribution models gain a measure of the total stellar masses. The stellar masses are of course connected to the luminosity, since it is derived from the light distribution. The metallicity is related to the luminosity and therefore also the stellar mass. This metallicity estimated from the stellar mass of the galaxy is thus also related to the metallicity of associated DLA by some parameter(Møller et. al 2013). This parameter is a function of the impact parameter and the metallicity gradient. The gradient has been estimated via applying this method on known DLA-galaxy pairs and has shown a metallicity gradient of -0.022 ± 0.002 dex/kpc(Christensen et al. 2014).

13 Searches for DLA counterparts

There has succesfully been found DLA galaxy counterparts via searching for Lyα emission at approximately the same redshift as the absorber. This method, however, has some obstacles, eventhough most of the quasar light near the Lyman α of the galaxy is extinquished by the DLA. The main problem is that the galaxies are often too dim.
As explained in section 7.1 DLAs with large EW of the Si II 1526 line has high metallicities. Because of the luminosity-metallicity relation the absorbing galaxy might also have a high luminosity. This makes this large EW_{1526} DLAs more likely have observable Lyα emission as well. This method has been shown to be succesful in several cases(Fynbo et al. 2010, Fynbo et al. 2011 and Fynbo et al. 2013).
One may also discover DLA-galaxy pairs by searching for galaxies with small impact parameter to a quasar sight-line(see section 2.6). This method is the one applied in this thesis.

14 Two low redshift galaxies with background quasars

For a part of this thesis the two spiral galaxies, NGC-4193 and UGC-08066, were investigated, see fig. 9 and fig. 10. The two galaxies were chosen as being candidate galaxy counterparts of DLAs. The main reason for choosing these were there proximity to a quasar sight-line. They were observed in January 2009 with the FOcal Reducer and low dispersion Spectrograph, FORS2, on VLT. In this thesis the metallicity across the galaxy are measued and metallicity gradients are estimated. By extrapolating the gradients the metallicity at the quasar sight-lines are predicted. The metallicites are estimated from simple line diagnostics. The actual metallicities at the quasar sight-lines should also be measureable in the quasar spectra via absorption lines. However, the lines used as metallicity measure are all in the UV part of the spectrum, along with Lyα which is also needed to be observed in order to conclude if they indeed are DLAs. Unfortunately, the only available spectra of these quasars are from ground based telescopes. Thus there are no measures of the quasar absorption lines investigated in this thesis.

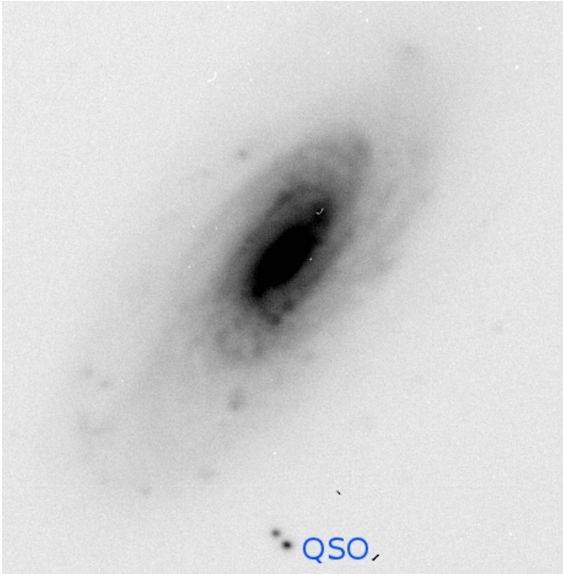

Figure 9: An acquisition image taking during observation, showing NGC 4193 and the background quasar. The sight-line of the quasar intercepts the galaxy 10.0 kpc from the centre.

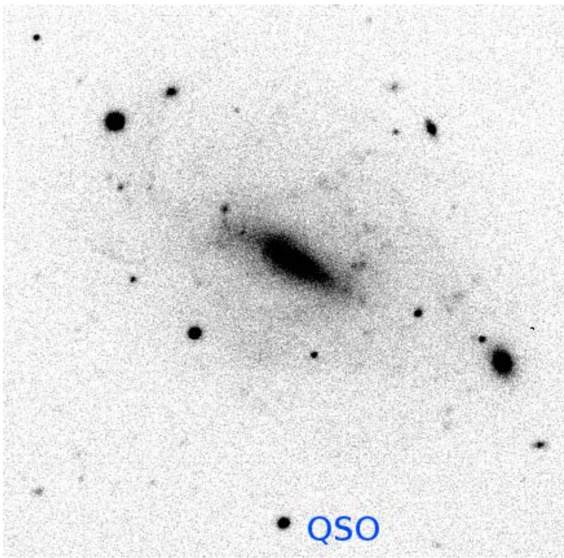

Figure 10: An acquisition image taking during observation, showing UGC-08066 and the background quasar nearby. The sight-line of the quasar intercepts the galaxy 9.8 kpc from the centre.

14.1 Background literature on the galaxies and quasars

Galaxy	z	σ_z	λ_{range}	Redshifted central λ			
				Hα	[N II] 6583	Hβ	[O III] 5007
NGC-4193	0.008272	0.000017	3500 – 8450 Å	6617 Å	6638 Å	4902 Å	5048 Å
UGC-08066	0.009226	0.000017	5120 – 8450 Å	6623 Å	6644 Å	4906 Å	5053 Å

Table 1: λ_{range} is the approximate redshift interval which is covered by the FORS2 spectra analysed in this thesis. This means that Hβ is not obervable for UGC-08066.

The two galaxies investigated in this thesis are NGC-4193 and UGC-08066, they have redshifts of $z = 0.008272$ $z = 0.009226$ respectively. In table 1 is listed the redshifted centre of the spectral lines which are focused on in this thesis. The two galaxies are both disk galaxies, but they are classified as quite different types:

- NGC-4193:
  It is classified as a Sbc galaxy, which is defined as a galaxy with quite loosely wound arms,

medium bulge, dust lanes and a bar(Baillard 2011).) In the database NED and SDSS it is classified as a normal star forming galaxy. However, in SIMBAD it is classified as an AGN. If it is in fact a AGN it should not affect the metallicity measurements significantly. But it will also be classified in this thesis by considering it in a BPT diagram. It is a member of the Virgo Cluster and has appeared in several surveys.

- UGC-08066:
  In SIMBAD this is classified as a low-surface brightness galaxy, LSBG. LSBG are more gas rich than normal spiral galaxies and have high mass-to-luminosity ratios. They probably have lower star formation rates due to a low surface density. The HII regions have low metallicities and in general LSBGs are less evolved than normal spirals. The neutral gas extends out to large radii and LSBGs are dark matter dominated and thus have very stable rotation curves(de Blok 2006).

The two quasars are in the SDSS database. For NGC-4193 the background quasar has identifier SDSS J121350.33+131057.8 and a redshift of $z = 0.959 \pm 0.00183$. For UGC-08066 the background quasar is SDSS J125703.67+010132.0 with redshift $z = 0.959 \pm 0.00169$.

The data for the galaxies is longslit spectra covering both the galaxy and the quasar. The data processing which was nessesary in order to analyse the spectra is described in Appendix D. The optical spectra of the quasar is not important in this study of the galaxy metallicity gradient, but the spectra have been processed as well and can be seen in Appendix E. However, it should be mentioned that a weak doublet absorption line, Ca II λ3934,λ3969, is seen for the redshift of the galaxy NGC-4193.

15 Analysis of the two low redshift galaxies

15.1 Emission line diagnostics

The method used to gain a measure of the metallicities across the galaxies is by using the simple line ratio indices N2 and O3N2. Using this method the spectrum do not need to be of the intrinsic flux. This is because they are both in a relatively short wavelength interval, and dust extinction significantly much with wavelength. Thus when taking the ration the extinction will be cancelledTo determine the integrated flux of the lines a Gaussian profile is fit to the lines. The instrumental and observational influences on the lines may be assumed to be the same for all lines and thus be they will be cancelled when taking the ratio. Even though, the lines are not resolved they still appear to have a Gaussian shape and a fit can be made. The most important parameter to keep constant when measuring the line ratios is the continuum level. Therefore the fits are done with a constant continuum for the two lines measured and all the other Gaussian profile parameters are free to vary. The IRAF/STSDAS task ngaussfit is applied to do the fitting. The continuum is chosen from a fit with continuum points not influenced by any clear skylines and other galaxy emission lines. The ngaussfit task calculate the associated error given the error spectrum as well it includes both the fitting error and the error spectrum to calculate errors on the fitting parameters. The parameters include the amplitude, FWHM and the central values along with errors on the slope and interception of the linear continuum fit.

15.1.1 Correcting for stellar absorption

Two methods are applied to correct for the stellar absorption which severely contribute to the spectra around the Hβ line. For most of the observed lines the equivalent width, EW of the absorption feature is simply assumed to be 2 Å. Thus the stellar absorption corrected flux, f_{corr} is added to the measured flux f_{meas}:

$$f_{corr} = f_{meas} + f_{cont} \cdot EW \tag{11}$$

Here the EW is scaled to the continuum flux f_{cont} around the absorption feature. The EW for an absorption line is in general defined to be positive, thus the corrected flux will be higher than the measured flux, as it ought to be.

But in some cases the Hβ line do not even reach above the continuum level, see figure 11 and thus a line fit cannot even be done. In these cases a Gaussian is instead first fitted to the stellar absorption feature. The absorption feature is then added to the spectrum. The Gaussian fit is done by avoiding the points in the spectrum which appear to be due to Hβ emission. By adding the Gaussian fit of the absorption the continuum around the emission line is evened out and thus the Hβ line is easily measured, see figure 11.

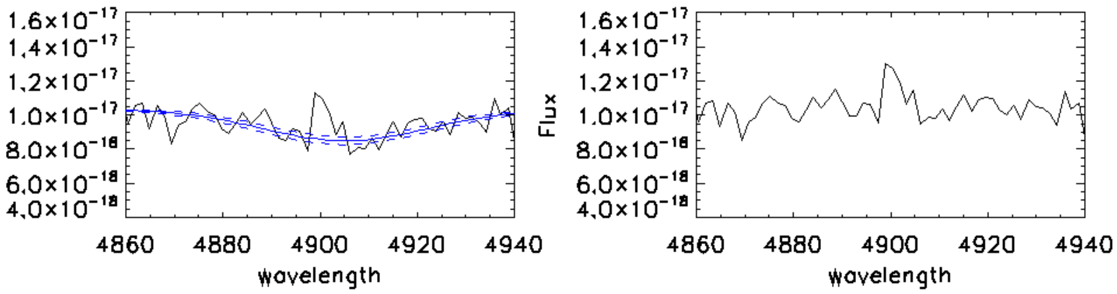

Figure 11: Stellar absorption correction in Hβ for NGC-4193 aperture 26. The left plot is for the original spectrum, the blue line is the Gaussian fit to the absorption feature. The blue dashed line is the 1σ for the Gaussian fit. The right plot is the corrected spectrum where the Gaussian fit is added to the original spectrum.

This last method described has only been valid to use for three apertures, number 10, 26 and 27 for the apertures towards the quasar sight-line. The aperture 26 and 27 have the largest radii where $O3N2$ was measurable and was therefore important to be included as well.

15.2 Metallicity gradient

To measure the metallicity gradients in physical sizes of the galaxies the angular sizes/distances for the apertures was converted to kilo parsec, see Appendix B. In figure 12 the metallicity gradient for N2 for both sides of the galaxy is shown. The two sides follow each other quite well until the outskirts of the HII emission regions of the galaxy. The metallicity is in general above solar values.

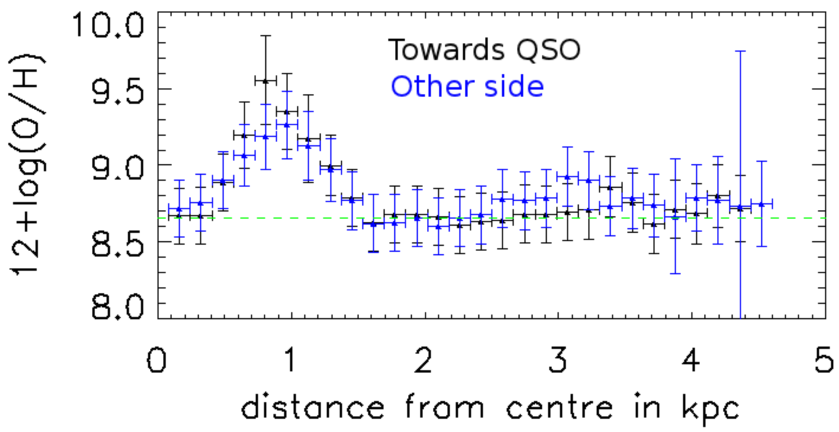

Figure 12: For NGC 4193: The metallicity measured via the measured N2 indices for both sides of galaxy. The green line indicate the solar metallicity, $12 + \log(\mathrm{O/H}) = 8.69$

The high N2 values approximately 1 kpc from the centre, may not indicate a high metallicity, see fig 13. In general the NII line starts to saturate when above solar values. Therefore when the nitrogen line becomes stronger than Hα, one must consider the high ionization to be due to something else than a possible high metallicity, e.g. shock ionization. Thus the N2 values above 1 are discarded, which result in a much flatter gradient.

For NGC-4193 there is also the possibility of measuring the O3N2 index in order to have another indicator of the metallicity, see figure 14. However, it was not possible for several apertures across the galaxy since either the Hβ or [OIII] line was not present. Perhaps due to extinction or high metallicity for the [OIII] line. Therefore there is not measured a better/alternative metallicity where the high N2 values was discarded. The two line ratios should in principle give the same metallicity since the relations used is are calibrated to the same data. They do differ a bit, but they are similar within the errors. There were actually no [O III] lines observable on the other side of the galaxy.

For UGC-08066 there was only data enabling [N II] λ6583, Hα O III λ5007 to be measured and not Hβ. Therefore the only indicator of the metallicity for this galaxy is via the $N2$ index. None of the N2 values is above 1(see figure 37 in Appendix G) and therefore all the measurements should thus be valid as a metallicity indicator. Therefore the $N2$ index is easily transferred to the metallicity, the result across the whole galaxy can be seen in figure 38 in Appendix G.

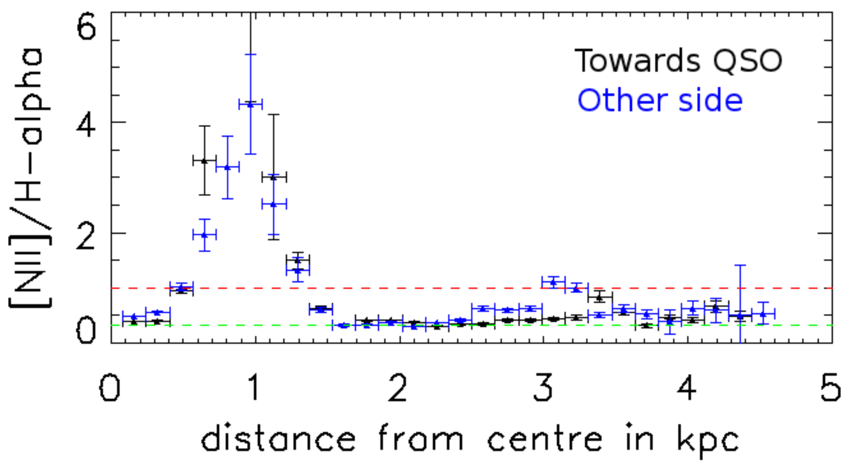

Figure 13: For NGC-4193: The N2 values measured for both sides of the galaxy is shown. The green line indicate the value which will give a corresponding solar metallicity, 12+log(O/H) = 8.69.

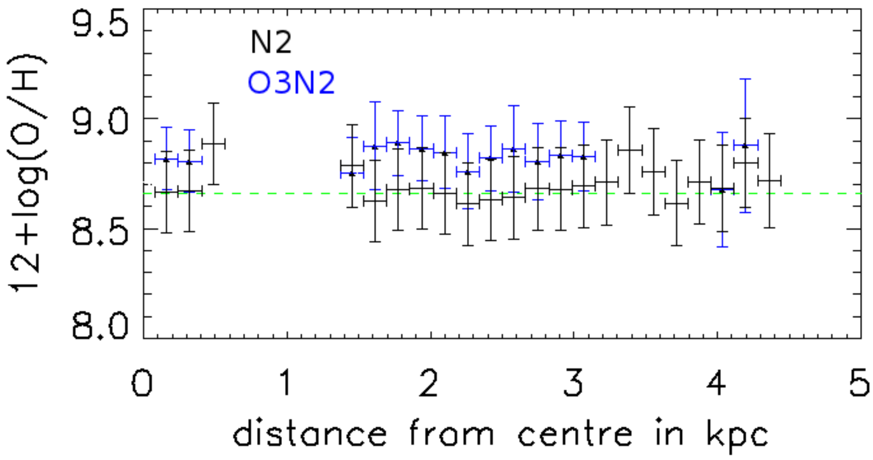

Figure 14: NGC-4193. This plot only shows the radial metallicity in the direction of the quasar sight-line. The black points indicate the metallicity measurements from the N2 index. The blue points indicate the metallicity measurements from the index O3N2.

15.3 Binning and extrapolating out to the quasar sight-line

The data is binned into 3-4 bins. This is done since the apertures which are measured are small compared to the seeing. This means that the light from one aperture is really spread across the neighbouring apertures as well, and the measurements are thus not independent. Therefore bins where chosen to include at least four apertures for NGC-4193 and two for UGC-08066. However, the last/farthest, relative to the centre of NGC-4193, measured O3N2 index was the only aperture in that area which was possible to measure. Since it is the measure closest to the quasar sight-line it is included in the fitting. The gradient for NGC-193 is quite flat and the most appropriate prediction to make is that it will continue to be essentially flat, at least out to the point where the quasar intersects. Therefore there is fitted a linear function to the binned data points, see fig. 15.

For UGC-08066 the only available line ratio to acquire the metallicity from is via the N2 index. For this metallicity gradient is also fitted a linear function, as seen in fig. 16. This shows the same flat metallicity gradient as seen across NGC-4193.

15.4 Velocity gradient

The shift of the central wavelength relative to the line centre of the galaxy is also measured. This wavelength shift is converted into a velocity. The velocity gradient for NGC-4193 is seen in figure 17 These velocities relative to the central velocity is a measure of the rotation of the galaxy disk. Galaxy disks do have flat rotation curves. Thus large deviations from a flat gradient might be due to something else than the rotation of the galaxies. The velocity shifts are measured for Hα since it in general is the line with the highest S/N.

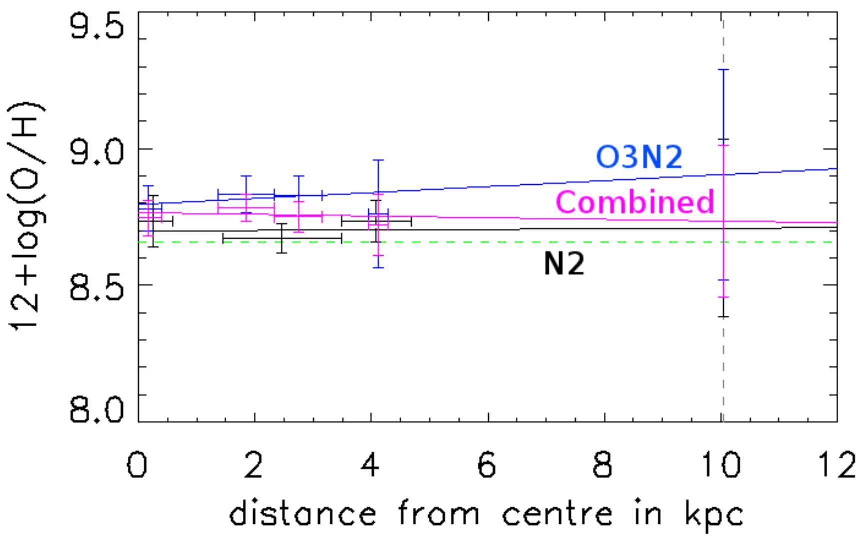

Figure 15: This figure contains the linear fits to binned metallicity measurements for NGC-4193. The grey dashed line indicate the distance out to where the quasar sight-line intercepts, 10.04 kpc.

	index	side of galaxy	intercept *12+(O/H)*	gradient *(12+(O/H))/kpc*	metallicity *12+(O/H)*
NGC-4193	N2	towards QSO	8.7 ± 0.088	0.00010 ± 0.031	8.7 ± 0.32
		other side	8.7 ± 0.09	0.0081 ± 0.034	8.8 ± 0.36
	O3N2	towards QSO	8.8 ± 0.079	0.011 ± 0.037	8.9 ± 0.38
	Avg. of both	towards QSO	8.8 ± 0.061	-0.0031 ± 0.027	8.7 ± 0.28
UGC-08066	N2	towards QSO	8.6 ± 0.13	-0.032 ± 0.080	8.2 ± 0.79
		other side	8.7 ± 0.11	-0.082 ± 0.039	7.9 ± 0.39

Table 2: Table containing fitting results for the metallicity gradients.

15.5 Balmer decrement and extinction

The colour excess in the B and V band, $E(B-V)$ might be measured from the line ratio of Hα and Hβ. The IDL routine get_ebv.pro[2] was used to convert from the measured line ratios to $E(B-V)$ values using the default settings. This result is seen in figure 18. It is non-physical that $E(B-V)$ is negative, therefore the dashed line at zero is a lower limit for the measurements of $E(B-V)$.

15.6 BPT diagram

The line ratios across the galaxy has also been plotted into a BPT diagram, see figure 19. This is again only for NGC-4193 since there is no observable Hβ in UGC-08066. The central aperture values are just at the line separating normal star forming galaxies from AGNs. Two of the lines are more into the AGN region. Since they are not in the central part of the galaxy it might be a sign of shock ionization.

16 Analysis of the DLAs in the X-shooter Large Programme

16.1 Determining redshifts

The redshift of the absorber is not determined from the Lymanα line since this is too broad for DLAs. Metal lines are much weaker and from them the line centres are more precisely determined. The most suitable metal lines to calculate the redshift from are redwards of the quasar Lyman α line. Here the lines avoid being blended with lines in the Lyman α forest.
In practise an approximate redshift is measured from the centre of the DLA, determined by eye.

[2] `http://idl-moustakas.googlecode.com/svn-history/r688/trunk/impro/pro/dust/get_ebv.pro`

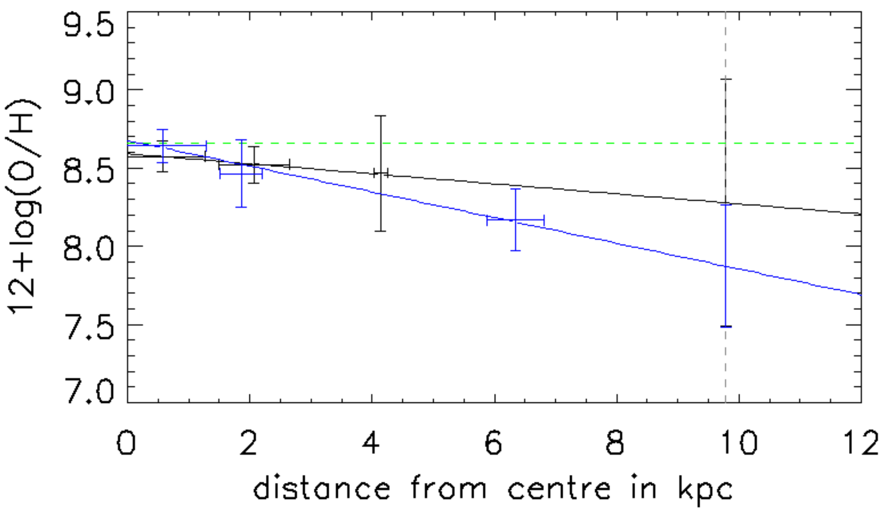

Figure 16: Here is shown the linear fit to the measured metallicity of UGC-08066. The grey dashed line indicate the distance out to where the quasar sight-line intercepts, 9.79 kpc. The black points are for the metallicity towards the quasar and the blue is for the other side of the galaxy.

Values for metal lines found in Lyman limit systems are redshifted the same amount as this and searched for at higher wavelength than the quasar Lyman α line. A DLA is a high column density LLS, and all the lines should be able to be present in a DLA spectrum. Since there is also searched for sub-DLAs the LLS metal list is more suitable.
When the lines are identified the central wavelength are measured from the most well defined lines. That means lines not blended with other absorption lines. The values of all th well defined lines are measured by fitting a Gaussian. However, sometimes all the lines appear to be blended. In these cases the absorber must consist of more components/absorbing clouds. A Gaussian is not appropriate to fit for these cases. Instead the central wavelength is found as the power-weigted mean wavelength, where the power $p(\lambda)$, is the spectral value:

$$\lambda_c = \frac{1}{P_{total}} \int_{\lambda_1}^{\lambda_2} p(\lambda)\lambda d\lambda \tag{12}$$

Here λ_1 and λ_2 are the two points where the line meets the continuum. It is normalized to the total power, $P_{total} = \int_{\lambda_1}^{\lambda_2} p(\lambda)d\lambda$.

Sometimes it is two close absorbers which make one large DLA feature, and the metal lines then show a clearer separation, making one able to distinguish them and determine two redshifts, one for each absorber. For these close absorbers the clearest metal lines are chosen, which makes it possible to fit the two lines with Gaussian profiles. The Gaussian profile fitting of two separated metal lines are done simultaneously. The simultanous fitting makes sure that there is accounted for line profiles which interfere with each other.

16.2 Continnum fitting

The fitting of the DLAs is in principle simple, since the Voigt function is a simple function, which for this purpose only is a function of column densities. The correct redshift is already measured before fitting and compared to how broad the DLA feature is, the error on the redshift is negligible. But there are many complications concerning the fitting, mainly the continuum fitting and where the DLA is situated in the quasar spectrum and the influence from other absorbers.

The DLAs are situated in the middle of the Lymanα forest, which is significantly dense for higher redshift quasar and becomes an issue when determining the placement of the continuum spectra. In order to do a proper fit for the DLA mainly the highest points in the forest are chosen, the 'tree tops'. The continuum fitting is done interactively in IRAF. Another complication when fitting is the location of the DLA in the quasar spectrum. A quasar spectrum is quite well known, and the continuum of the quasar is a simple power law. But besides the continuum spectrum, there are also significantly broad emission lines.
If a DLA is near a dominant broad quasar emission lines, e.g. the Lymanβ line, a quasar

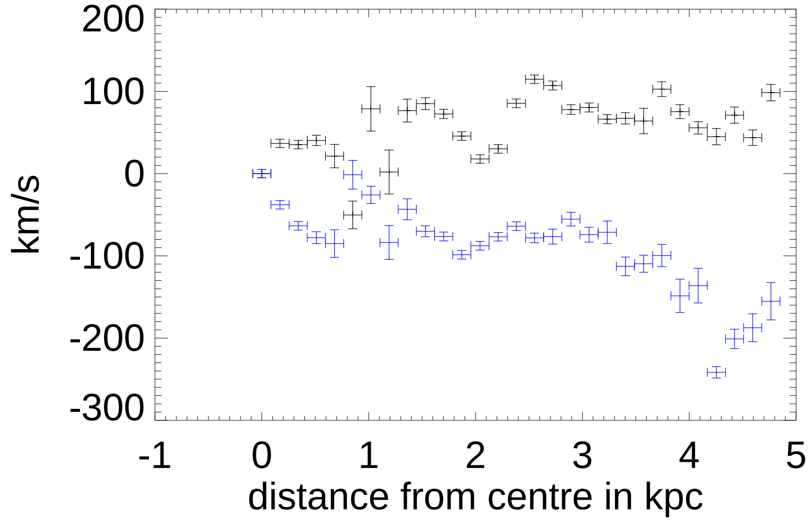

Figure 17: These measurement are of NGC-4193. Here is shown the velocity shift across the galaxy relative measured from Hα. The black points are in the direction of the quasar sightline interception and the blue points for the other side of the galaxy. The velocities are set relative to the central aperture value.

composite template spectrum is used to help determine where the unabsorbed continuum might have been. The quasar composite spectrum is constructed as an average quasar spectrum from several observed spectra, see figure 20. The largest difference between the composite spectrum and an observed spectrum is the broad emission lines. They are flattened out in the composite spectrum and do thus not have a high central peak. In this quasar sample the broad emission line strengths do vary a lot from thelines in the composite spectrum. Therefore the composite quasar template is used as a very rough outline of the possible continuum. Since the template in general is a bad representation of the centre of the broad lines, the continuum fitting are for the most dominant broad lines done by avoiding the centre of the line. Therefore a residual of the broad lines are sometimes still visible in the normalized spectrum(e.g DLA J0424-2209 z=2.983). These residuals will be avoided in the fitting of the DLA.

16.2.1 At Lyman break

There was not found any absorbers near a complete Lyman break in the sample. However, a few DLA lines was in partial Lyman breaks. Thus the continuum level is different on each side of the the DLA and two continnum fits was done. The two normalized spectra was combined at the points where the Lyman break should occur according to the redshift of the Lyman break absorber. Due to the significantly lower flux level bluewards of the DLA the noise is also higher. Therefore the most important part of the spectrum in the fitting is redwards of the line. Because of the lower error the best fit will mostly rely on the continnuum fit of this redder part, see e.g. the DLA observed at a redshift 2.30 in the quasar J1024+1819 in figure 43 in Appendix G.

16.3 Voigt profile fitting of DLAs

When the spectrum is properly normalized properly it is easy to fit the DLA. The DLA is fitted with a Voigt profile with the neutral hydrogen column density, N_{HI} as the only free parameter, since the redshift is already determined and the doppler width is set to $b = 10\,km/s$. This is lower than median value for DLAs. However, it has been tested for both a high and low N_{HI} absorber how this effect the fitting. From the test it was concluded that there was no significant changes the profile shape for $b < 100$ km/s. For the high N_{HI} absorber, it was for significantly higher $b < 100$ than any changes occured.

χ^2 statistics are used to determine the best fit. Several profiles with a column density values inside an interval are fitted to the DLA profile. The interval is determined by eye for which it appear to cover the fit with the lowest and highest possible column density. The fit with the reduced χ^2 closest to one is chosen as the best fit.
To be more certain that the chosen fit is in fact the correct/best it is compared to the second

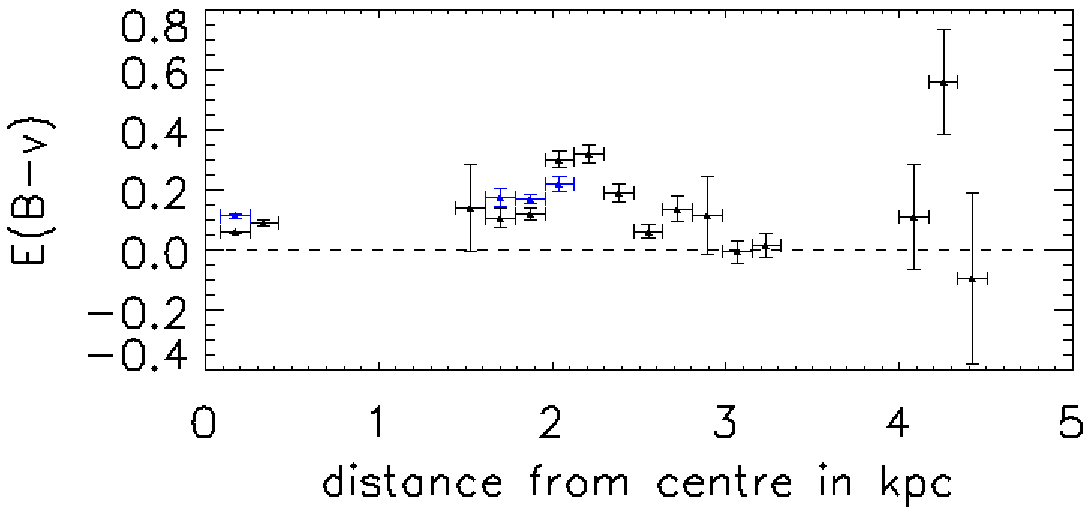

Figure 18: E(B-V) measured from the Balmer decrement for NGC 4193. The black points are for the side of the galaxy towards where the background quasar intercepts, and the blue are for the other side of the galaxy

best and third best fit. The fit is expected to converge towards the best fit. A way of missing the minimum chi-squared is by not having a sufficient number of column densities in the interval. If there is not a sufficient number of column density a wrong best fit might be found. Thus the first iteration is done by having a fair low spacing between the fitted column density values, in order to avoid finding a wrong minimum. Luckily it is easy to see if the fit is really off and the best fit is incorrect, so this method seems solid for this purpose.
When it is shown that the Voigt profile fitting converges towards a certain column density, a second fitting is done, closing the interval around this column density, and making the spacing between the tested column densities even smaller. The spacing between the column densities chosen here corresponds to the precision of the fitting, and thus the spaces should be smaller than the measurable column density.

16.3.1 Close absorbers

When two absorbers are so close to each other that the wings overlap, see e.g. fig 21, one has to account for this, since there will be more absorption in the overlapping wings, and thus a fit to each of the DLAs separately will not be correct. Two absorber might even be so close that the core of the Voigt profile overlap and the two actually appear as one feature. These are cases where one might have to fit the two DLAs simultaneously.

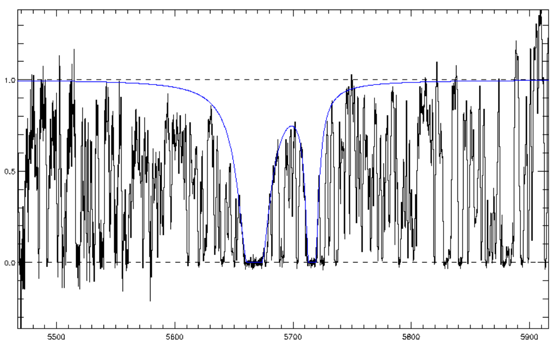

Figure 21: An example of Voigt fits for two close absorbers.

The method used to fit the two absorbers at the same time is by multiplying two Voigt profiles, one for each absorber. The combined profile is then fitted to the combined absorption feature.
When applying this method for two very close absorbers where the cores overlap, it is one of the two which end up dominating the entire fit. The best fit converges towards one of the absorbers gaining higher N_{HI} and the other becoming negligible. Thus this method does not seem to work for these cases. The only two close DLAs which did converge towards a minimum was in the quasar spectrum J0034+1839. They were, however, not as close as each other with a redshift separation

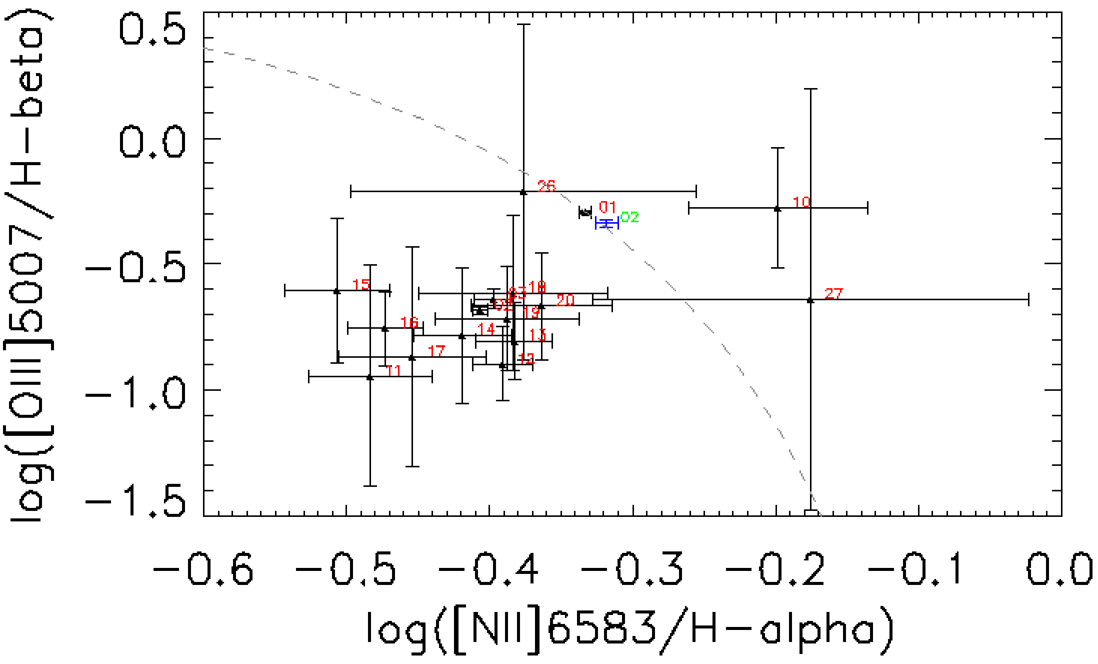

Figure 19: The BPT diagram for NGC 4193, with increasing number meaning a larger radial distance, out towards the quasar. The blue point is for the single point on the other side of the galaxy, the aperture just next to the centre.

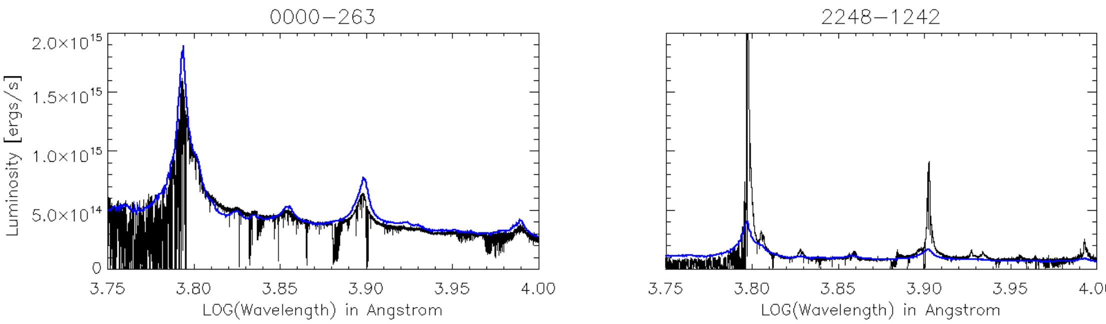

Figure 20: The qso composite spectrum(blue) compared to two of the sample quasar spectra.

of $\Delta z = 0.3$. However, for all cases it does show that by fitting them separately the total N_{HI} (the sum of the two best fit N_{HI} values) is lower than if only one profile is fitted. Therefore the N_{HI} inferred from the fitting of the absorption as a single line might only be an upper limit for the actual amount of neutral hydrogen. The question is if these close absorbers are 'real' DLAs. Do they contain a high percentage of neutral hydrogen, or perhaps one or both of them are merely sub-DLAs?
However, since it could not be shown that it was indeed two different absorbers by fitting separate profiles simultaneously. They are assumed to be normal DLAs. It may be a part of the more ionized gas at the outer parts of the absorbing clouds which show this splitting of the metal lines . But the actual separation in velocity space should be investigated further to tell, if this separation is also valid for the neutral gas.

16.4 The DLA sample

From the sample of 85 quasar spectra 64 absorbers has been identified, see figure 22. This sample includes 33 DLAs and 31 sub-DLAs(figure 23). All the fits done to obtain N_{HI} is shown in the figures 42, 43, 44 and 45 in Appendix G, and the results are in table 5 in Appendix H. The overall distribution of the DLAs ($N(HI) > 20.3$) do show a higher number of absorbers with low N_{HI} compared to the DLAs with high N_{HI}. This trend should of course also be seen in the sample of sub-DLAs, however, this is not detected. The very low sub-DLAs are missing, this is probably a bias from the analysis methods. They might have been excluded since they have not shown any clear damped wings. This is very likely since there is a high change for the wings to be 'lost' in

the Lyα forest.
The redshift of most of the absorbers are between $z_{abs} = 3 - 4$, as expected with this sample of quasars, see figure 23. When looking at the distribution of N_{HI} as a function of z, see figure 24, the most interesting feature is the lowest redshift part, where there is mainly identified DLAs and few sub-DLAs, in fact some of the highest N_{HI} DLAs of the sample. The low redshift is in the bluest part of this quasar sample, and is for many of the spectra the part with the lowest flux, and lowest S/N. This has in previous studies been shown to give an overestimation of the measured N_{HI}, and it looks like this might have occurred here as well.

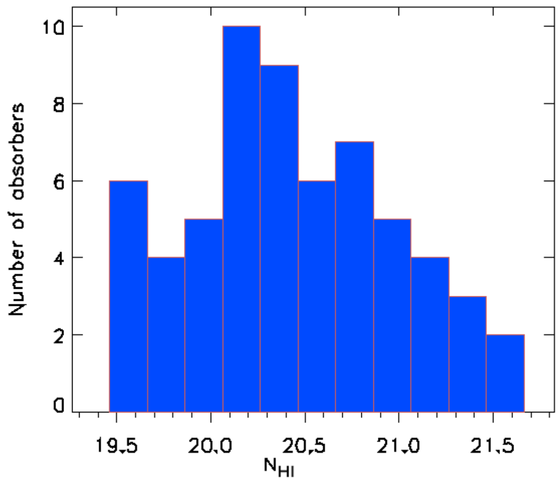

Figure 22: A histogram of the neutral hydrogen column densities, N_{HI}, of the identified absorbers.

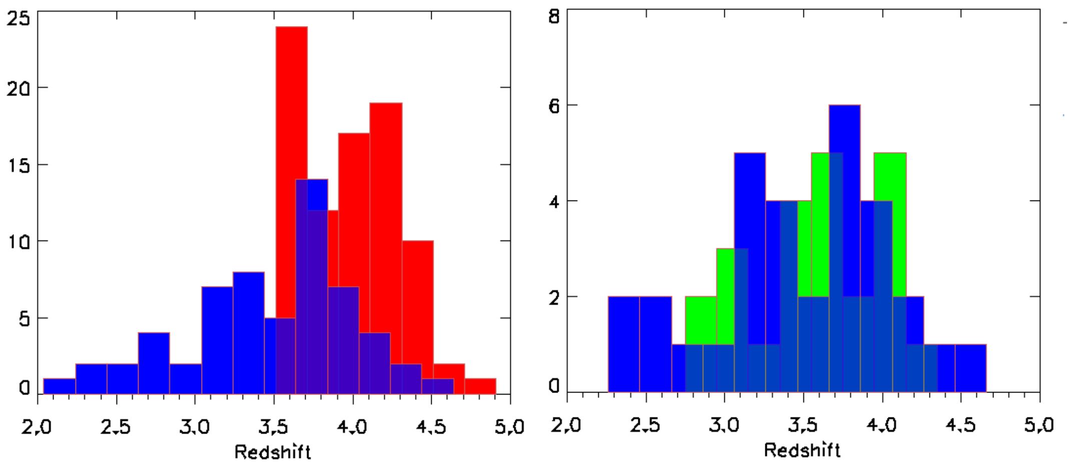

Figure 23: Histograms illustrating the number of identified DLAs(blue) and sub-DLAs(green) for the quasars(red) sample.

16.5 Equivalent width of Si II 1526

From the sample of identified absorbers the equivalent width of SiII 1526, $EW1526$, is measured from equation 16 in Appendix A. All the measured spectral lines can be seen in 39,40 and 41 in Appendix G. Many of the DLAs and sub-DLAs have no measurable Si II lines, they are e.g. in the forest or severely blended with other absorption lines. N_{HI} has been plotted as a function of equivalent $EW1526$ in figure 25. It is evident that there is a difference between the DLAs and the sub-DLAs. The results of converting $EW1526$ to the metallicity, $[M/H]$ via the power law relation between the two properties(equation 7) are shown in figure 26.There is a lot of points over the threshold for where Si II is very saturated. The metallicity has also been plotted as a function of redshift, see figure 27. As expected there does not seem to be any significant evolution during this short redshift interval and high scattering.

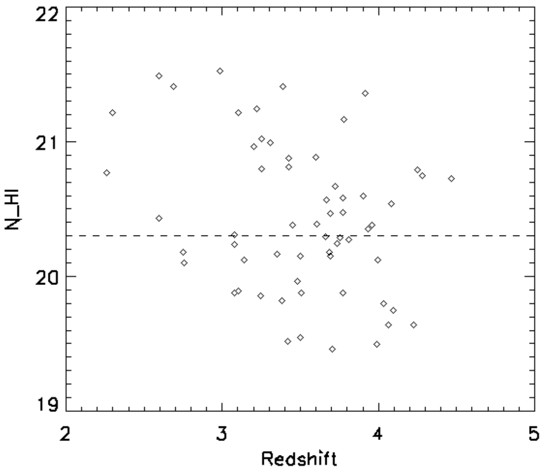

Figure 24: A plot of neutral hydrogen column densities, N_{HI}, as a function of redshift for the sample of identified DLAs and sub-DLAs. The horizontal dashed line indicate the N_{HI} limit for DLAs.

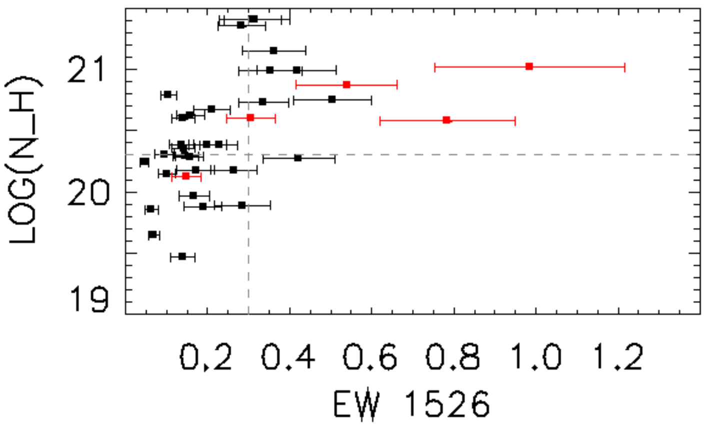

Figure 25: The neutral hydrogen column densities, N_{HI} as a function of the measured equivalent width of Si II 1526, EW_{1526}, for the identified sample of DLAs. The red points are for 'DLAs' for which the Lya absorption possible stem from two absorbers. The horizontal dashed line at 0.3 indicate where SiII 1526 starts to become highly saturated. The horizontal dashed line indicate the separation of DLA from sub-DLAs

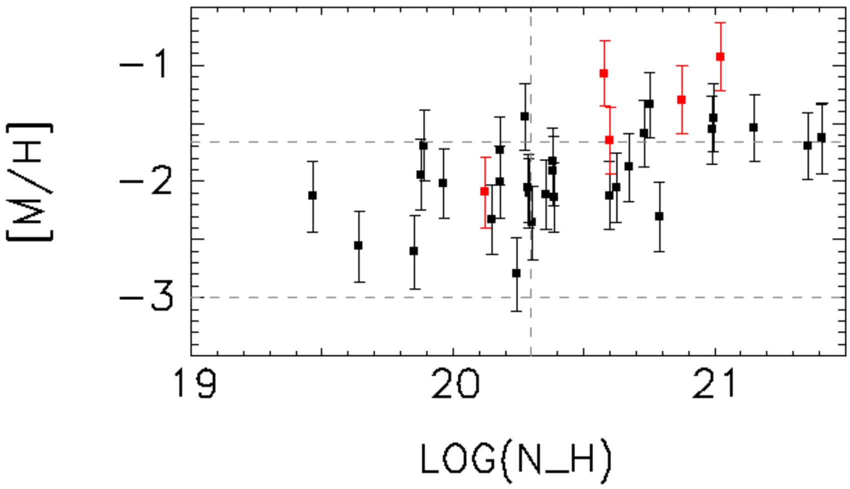

Figure 26: The metallicity measured for the DLAs and sub-DLAs where Si II 1526 is observable. The red points are for 'DLAs' for which the $Ly\alpha$ absorption possible stem from two absorbers. The upper horizontal dashed line at 0.3 indicate where SiII 1526 starts to become highly saturated. The line at [M/H]=-3 is the predicted metallicity floot. The vertical dashed line indicate the separation of DLA from sub-DLAs

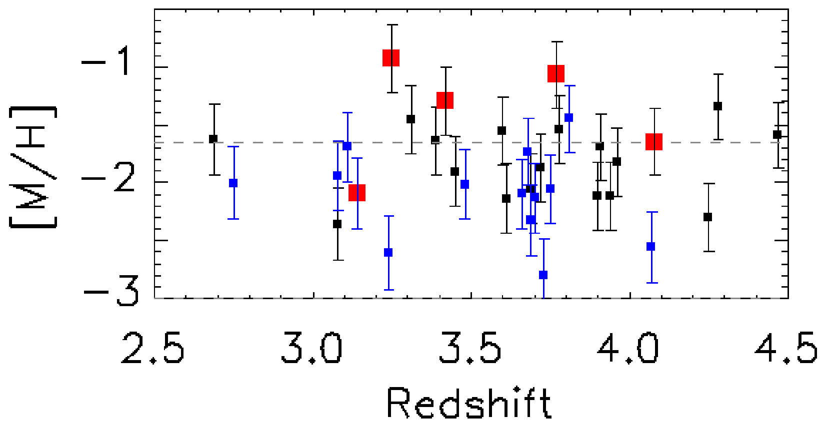

Figure 27: The metallicity as a function of redshift measured for the DLAs and sub-DLAs where Si II 1526 is observable. The black points are DLAs and the blue are sub-DLA. DLAs for which the $Ly\alpha$ absorption possible stem from two absorbers are indicated with a red square. The horizontal dashed line at 0.3 indicate where SiII 1526 starts to become highly saturated.

16.6 Estimating Ω_g^{DLA} for the DLA sample

The total path length, ΔX, has been calculated for all searched quasar spectra(equation 5). Only DLAs between 3000 km/s redwards of the Ly-β emission line and 5000 km/s bluewards of the Ly-α emission line has been included. This redshift path definition was partly determined since the same method was used for the newest SDSS DLA sample survey(Noterdaeme et al 2012). This method avoids the bluest part of the spectrum where it can be very difficult to determine where the continuum starts becoming too noisy. By choosing these upper and lower redshifts the most dominant quasar emission lines are also avoided. ΔX was calculated to be 213. For the chosen ΔX 21 out of the 33 identified DLAs are included in this sub sample. The cosmological mass density of neutral gas for the DLAs, Ω_g^{DLA} is 0.00167 ± 0.00069 and is plotted in figure 28.

,

17 Discussion of results

17.1 Metallicities of the DLA sample

From figure 25 it do appear as if there is a difference between the DLAs and sub-DLAs. The correlation between EW_{1526} and [M/H] was only made for DLAs, therefore it is not odd there

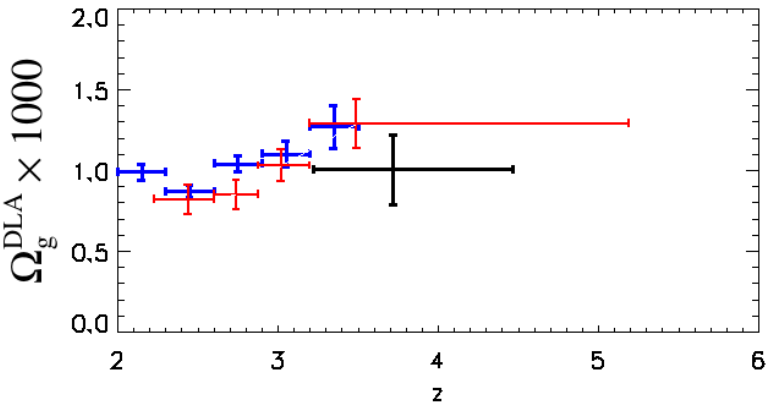

Figure 28: $\Omega_g^{DLA} 10^{-3}$ for previous studies and this. The black bins are the Ω_g^{DLA} for the X-shooter Large Programme sample, the centre of the redshift bin is for the median z, which is $z_m = 3.72$, the redshift bin is $z = [3.22, 4.47]$. The blue bins are for the newest SDSS data release, DR9, Noterdaeme et al. 2012. The red bins are for a previous SDSS release, DR7, Noterdaeme et al. 2009.

is this difference. It is possibly because of the higher ionization of sub-DLAs. Since sub-DLAs are less effective at shielding it is likely that higher ionization states are more important for Si. Therefore these metallicity measurement for sub-DLA is likely not their actual metallicity. All the absorbers which showed a clear separation of the metal lines do have a high metallicity. This is not surprising since the lines can grow longer without being affected by the high saturation level. These absorbers which have shown a separation of Si II 1526 has also been measured assuming it actually is two absorbers(5 in Appendix H). But since it has not been shown here that it is two absorbers a mean metallicity for the sample has been measured as if they are one DLA.
The mean metallicity for the DLAs has been measured from a sample of 21 out of the total sample of 33 DLAs. This results in a mean metallicity of [M/H]=-1.8 dex, this is in the low end of the very scattered metallicity distribution for DLAs. But for these redshifts it is not unlikely to observe.

17.2 Ω_g^{DLA}

The cosmological mass density of gas in DLAs, Ω_g^{DLA}, is in this thesis estimated to be 0.00167 ± 0.00069. This result is consistent with previous studies, see figure 28. This estimate is slightly lower than for other measurements at the same redshifts. It could be explained by the lack of high column density DLAs, $N_{HI} > 10^{22} cm^{-2}$. However, by including a high N_{HI} DLA the sample standard deviation will become larger as well.
The deviation from the literature measurements can also be due to 'incompleteness' of the sample. Some DLAs might have missed detection due to e.g. low S/N. However, the total path length was chosen to be in a generally high S/N part of the spectrum, and mainly the DLAs with the lowest N_{HI} are likely to be missing. These possibly missing low N_{HI} should not result in a significantly higher Ω_g^{DLA}. It appears as if this DLA sample has been mostly biased at low redshift(24) and with regards to the sub-DLAs. There should be run some simulations on the data to estimate for incompleteness.

17.3 Bar shocks in NGC-4193?

There are signs of shocks in NGC-4193 from both the high $N2$ index values(figure(13) and the points in the BPT diagram which surpass the AGN limit line(19). Given that the high $N2$ values are symmetric across the galaxy along with it being quite close to the centre it suggest that it might be due to the central galaxy bar(Baillard 2011). Bar shocks are expected to occur since there is a gas inflow along the bar. The gas flow is from gravitational torques produced by the bar(Sparke, L.S & Gallagher). From the image of the galaxy in figure 29 it is clear that the regions are in fact at the edge of the bar.
Further measurable properties which can also show if it is a shock is the velocity shifts of the emission lines(17). There are in fact jumps in velocity in the order of $50 - 100 km/s$ in the region. Jumps of these sizes are expected from simulations of weak barred potentials perpendicular to the disk(Athanassoula 1992) and observed through HI(Mundell & Shone 1997). However, these measurements are unfortunately for the HII emission lines which are not optimal at tracing the gas velocity. HI maps or maps of the molecular clouds via CO(e.g. Reynaud & Downes 1996) would

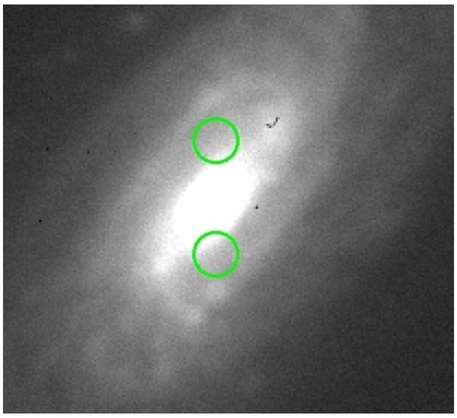

Figure 29: Here is the same acquisition image of the galaxy NGC-4193 as seen in figure 9, this image is zoomed in near the bar. The two circles indicate where the shocks was observed(aperture 5-9) for both sides of the galaxy. Assuming the lightest part is the bar, the regions are just at the edge of the bar with a radial distance of ~ 1 kpc.

be more suited. Bar shocks are expected to be related to dust lanes and jumps in velocity has been observed across the lanes (Kormendy 2004). From the Balmer decrement measurements(18) it do appear as if their is high extinction in this region, since the Hβ line is not observable at all. So the slit probably do cross a dust lane. From the observations analysed in this thesis it cannot be concluded that it is in fact bar shocks, since no proper measure of a velocity shift is available. However, it is very likely that this is the case since there are signs of shock ionization and the regions are near the edge of the bar.

17.4 The galaxy gradients

The measurements of the galaxy gradients show rather flat metallicity gradients(2). This is consistent with other metallicity measures of local galaxies. Even though the metallicity gradients appear to be flat they might decline further out in the galaxy before reaching the quasar sight-line. As seen for UGC 08066 in figure 38 and in the 2D spectrum(figure 33) there is a clear emitting point at the other side of the galaxy over 6 kpc away from the galaxy centre, a few kpc further out than the other measurements. This measurement show a lower metallicity than the points closer to the centre. Therefore the gradient has also been measured for this side of the galaxy. As seen in table 2 this gradient is steeper than all the other measurements. But what this extra point actually do is confining the gradient to be in the lower half of the 1 σ errors when comparing to the other side of the galaxy. However, it is still not a very steep gradient.

17.5 The metallicity at the quasar sight-line

The fact that both of these galaxies show metallicities around solar along with the flat metallicity gradients give the result of solar values at the quasar-sight line as well(2). This means if these galaxies actually are DLA counterparts, the DLA at the quasar sight-line will have a solar metallicity. As mentioned in section 6 most DLAs do have low metallicities, these results therefore predict that if these galaxies are absorbers they will be in the very high end of the metallicity regimes for DLAs.

18 Future prospects

The original plan for NGC-4193 and UGC-08066 were to follow up with ultra violet observations of the background quasars. The results acquired in this thesis indicate that the two galaxies might be DLA-candidates given the possible high metallicity at the quasar sight-line. Previous high metallicity quasar-galaxy pairs have shown to have even larger impact parameters(16 kpc Fynbo et al. 2013) than for these two cases. It is therefore not found unlikely that NGC-4193 and UGC-08066 can be high metallicity absorbing galaxies as well.
Given there is a sign of the Ca II doublet in the background quasar for NGC-4193, this is probably more likely to a high metallicity absorbing system than UGC-08066.
The galaxy NGC-4193 show clear signs of bar shocks and it will be possible to e.g. acquire HI maps of the galaxy to further study its velocity structure.

19 Conclusion

The two low redshift galaxies, NGC-4193 and UGC-08066, have both been shown to have quite flat metallicity gradients. For both galaxies solar metallicities are measured in the HII regions. These results imply possible high metallicity absorbing galaxies. Further observations of the background quasar are needed to confirm this.
Signs of shock ionization in NGC-4193 via the $N2$ index has been shown. This ionization seems to be consistent with being caused by the dynamics of the galaxy bar.
In the large quasar sample from the Large VLT/X-shooter Programme a sample of 33 DLAs has been identified. A third of these were used in the calculations of the cosmological mass density of neutral gas in DLAs, Ω_g^{DLA}. This sample has a redshift range of $z = [3.22, 4.47]$ and give Ω_g^{DLA}=0.00167 ± 0.00069, consistent with previous studies.
The mean metallicity of the whole sample was found via the relation between the equivalent width of SiII 1526 and [M/H]. From measurements of 21 of the DLAs a mean metallicity was found to be [M/H]=-1.8 dex.

References

Asplund, M., Grevesse, N., Sauval A.J. & Scott, P. AA&A, 2009. 47, 481
Athanassoula, E., 1991 MNRAS, 1992, 259, 345
Baillard A. ,2011, A&A 532, A74
Baldwin, Phillips & Terlevich, 1981, PASP, 93,5
Braun, R. 2012, ApJ, 749, 87
Chen, H-W., 2005,astro-ph/0410558
Chen, H-W., Kennicutt, R. C., Jr., & Rauch, M. 2005, ApJ, 620, 703
Christensen, L., Møller, P. , Fynbo, J.P.U. & Zafar,T. ,2014,arXiv:1404.6529
de Blok, E., *Low Surface Brightness Galaxies* , IOP Publishing Ltd, (2006)
Dessauges-Zavadsky, M., Péroux, C., Kim, T.-S., D'Odorico, S., & McMahon, R. G. 2003, MNRAS, 345, 447
Ferguson, A. M. N., Gallagher, J. S., & Wyse, R. F. G. 1998, ApJ, 116, 673
Fitzpatrick, E. L., 1999, PASP, 111,63
Fynbo, J. P. U., Laursen, P., Ledoux, C., et al., 2010, MNRAS, 408, 2128
Fynbo, J. P. U., et al. 2011, MNRAS, 413, 2481
Fynbo, J. P. U., et al. 2013, MNRAS, 436, 361
García, T. T, 2006, MNRAS, astro-ph/0602124v2
Ellison et al., 2010, MNRAS, 406, 1435
Emerson, D., *Interpreting Astronomical Spectra*, John Wiley & Sons Ltd, 1996, Chapter 6
Ferland, G. J. et al., 2013, *Release of Cloudy. Revista Mexicana de Astrnomia y Astrofisica*, 49,1-27
Haehnelt, M. G., Steinmetz, M., Rauch, M., 1998 ,ApJ, 495,647
Henry, R. B. C. & Worthey G., 1999, PASP, 111, 919
Hogg, D.W.,*Distance measures in cosmology*,2000,astro-ph/9905116v4
Hopkins,A. M., McClure-Griffiths N. M. & Gaensler, B. M., 2008, ApJ, 682, L13
Jones T., Ellis R. S., Richard, J. & Jullo E. ,2013 ,ApJ, 765, 48,
Kaplan, K. F., Prochaska J. X. Herbert-Fort, S., ELLISON, S. L. & Dessauges-Zavadsky M., 2010, PASP, 122, 619
Kauffmann et al., 2003 MNRAS, 346, 1055
Kewley, L. J. & Ellison, S. L., 2008, ApJ, 681, 1183
Kennicutt, R. C., Jr. 1998, ApJ, 498, 541
Kormendy 2004, arXiv:astro-ph/0407343 Longair, M. S., *Galaxay formation(2nd edition)*, A&A Library, Springer, 2008, Chapter 18
Krogager, J.-K., et al. 2013, MNRAS, 433, 3091
König, B., Schulte-Ladbeck, R. E. & Cherinka, B. 2006, 132, 1844
Møller, P., Fynbo, J. P. U., Ledoux, C., & Nilsson, K. K. 2013, MNRAS, 430, 2680
Mundell, C. G. & D. L. Shone , 1999, MNRAS, 304, 475
Murphy, M. T.,Curran, S. J., Webb, J. K., M énager H. & Zych B. J., 2007, MNRAS, 376, 673
Noterdaeme, P., Petitjean, P., Ledoux, C., & Srianand, R. 2009,A& A, 505, 1087
Noterdaeme, P. et al., 2012, A&A 547, L1
Osterbrock, D. E., *Astrophysics of Gaseous Nebulae and Active Galactic Nuclei*, 1989 ,University Science Books, Mill Valley, CA,
Péroux, C., Bouché, N., Kulkarni, V. P., & York, D. G. 2013, MNRAS, 436, 2650
Pettini, M., *Element Abundances through the Cosmic Ages*, 2003,astro-ph/0303272
Pettini, M. & Pagel, B. E. J., 2004, MNRAS, 348, L59
Prochaska J.X., Herbert-Fort S & Wolfe A. M., 2005, ApJ, 635, 123
Prochaska J.X., Chen, H. W., Wolfe A. M. Dessauges-Zavadsky, M. & Bloom. J.S., 2008, ApJ, 672, 59
Prochaska, J. X., & Wolfe, A. M. 2009, ApJ, 696, 1543
Rafelski, M., Wolfe, A. M., Prochaska, J. X., Neeleman, M., & Mendez, A. J., 2012, ApJ, 755, 89
Rao, S. M., Turnshek, D. A., & Nestor, D. B. 2006, ApJ, 636, 610
Reynaud D. & Downes D. 1996, A& A, 319, 737
Rupke, D. S. N., Kewley, L. J., & Barnes, J. E. 2010a, ApJL, 710, L156
Rupke, D. S. N., Kewley, L. J., & Chien, L.-H. 2010b, ApJ, 723, 1255
Sparke, L.S & Gallagher III, J.S., *Galaxies in the Universe: An introduction(2nd edition)*,Campbridge University Press, 2007, Chapter 5
Telfer, R. C., Zheng, W., Kriss. G. A. & Davidsen, A. F.
Tripp, T. M. & Bowen D. V. 2005, in William P., Shu C.G. & Menard B., IAU Colloq. 199, *Probing Galaxies Through Quasar Absorption Lines*,Cambridge University Press
Tremonti, C. A. et al.,2004 ApJ, 613, 898
Yuan, T ,Kewley, L. J. , Swinbank A. M. & Richard, J., 2012, ApJ, 759 ,66
Westmoquette, M., Clements, D., Bendo, G., & Khan, S. 2012, MNRAS, 424 ,416
Wise, J. H., Turk, M. J., Norman, M. L., & Abel, T. 2012, ApJ, 745, 50
Wolfe, A. M., Gawiser, E., & Prochaska, J. X. 2005, ARA&A, 43, 861
Wright, S. A., Larkin, J. E., Graham, J. R., & Ma, C.-P. 2010, ApJ, 711, 1291
Zwaan, M.A., van der Hulst, J. M. , Briggs, F. H. , Verheijen, M. A. W. ,Ryan-Weber, E. V., 2005, MNRAS, 364, 1467

Appendices

A Equivalent width, EW

If the spectral resolution is smaller than the line width, the line can be resolved and a line profile function can be fit to obtain the FWHM, central wavelength and amplitude. If the spectral resolution is larger, the line will appear different than the intrinsic profile and a correct measure of the line profile parameters is not possible. However, there will even for a full resolved line be an artificial broadening due to the instrument. This instrumental FWHM$_{instr}$ needs to be subtracted from the measured FWHM$_{meas}$ as, FWHM$^2_{meas}$−FWHM$^2_{instr}$. A unresolved line will smoothen out, meaning the measured amplitude will be lower than the intrinsic and the FWHM will be larger.

The EW is independent of the spectral resolution and is therefore used instead of a line profile function. Since the line is spread out if the resolution is not sufficient, a saturated line might appear unsaturated. An absorption line observed to have an amplitude half of the continuum can actually be saturated if the spectral resolution is low. But the equivalent width is invariant eventhough the line is saturated.

The definition of the equivalent width:

$$EW_\lambda = \int_{\lambda_1}^{\lambda_2} (1 - F_\lambda/F_0) d\lambda \tag{13}$$

Here F_λ is the spectral values, e.g. the flux and F_0 would then be the continuum flux. The integral covers the wavelengths of the spectral line, which starts at λ_1 and ends at λ_2. It is easier to work with an absorption line if the spectrum is normalized to the continuum. If it normalized the equivalent width is a bit simpler:

$$EW_\lambda = \int_{\lambda_1}^{\lambda_2} (1 - F_\lambda) d\lambda \tag{14}$$

For a normalized spectrum the EW is essentially a value for the width of a rectangle with unity height which have the same area as the integrated spectral line.

For a real spectrum it is of course digitialized and the wavelength inverval/dispersion, $\Delta\lambda$ is often too large for integration. Instead one use a sum over the normalized flux values. The digitilized equivalent width is thus[3]:

$$EW_\lambda = \sum_{\lambda_1}^{\lambda_2} (1 - F_\lambda)\Delta\lambda \tag{15}$$

The wavelength interval,$\Delta\lambda$, is not changing much over a single line an can be set as constant, e.g. as the average interval for all the wavelengths the line covers:

$$EW_\lambda = \left(\frac{\lambda_2 - \lambda_1}{n_\lambda}\right) \sum_{\lambda_1}^{\lambda_2} (1 - F_\lambda) \tag{16}$$

Here n_λ is the number of points/pixels values summed.

For the lower limit of N_{HI} for DLAs($2 \cdot 10^{20}\, cm^{-2}$) the equivalent width is 10 Å, for sub-DLAs it is 2.5 Å. EW measured for a redshifted line have been broadened due to the cosmological expansion. The rest frame equivalent width, EW_0, is merely the observed EW divided by a factor $(1 + z_{abs})$. Therefore DLAs observed at a high redshift do also have EW even larger than 10 Å. DLAs observed from the ground will have $EW \geq 16$ Å, since the atmospheric cutoff is at $\lambda = 3200$Å(Pettini et al. 2003).

[3]The equation is from lecture notes from a course, *Astronomical Data Processing*, provided by the University of Copenhagen. The notes are written by Peter Jakobsen)

B Cosmological parameters and calculations

For this thesis is applied a ΛCDM cosmology for a flat universe with $\Omega_\Lambda = 0.7$, $\Omega_m = 0.3$ and $H_0 = 70\,kms^{-1}Mpc^{-1}$.
For the calculations of the cosmological mass density of neutral gas in DLAs, Ω_g^{DLA} the current critical mass density, ρ_c, is applied in equation 6. ρ_c is simply defined as:

$$\rho_c = \frac{3H_0^2}{8\pi G} \tag{17}$$

Where G of course is the gravitational constant, $G = 6.67 \cdot 10^{-8} cm^3 s^{-2} g^{-1}$. The Hubble constant in cgs units is $H_0 \approx 2.3 \cdot 10^{-18} s^{-1}$.
It is rather low redshift galaxies and the expansion of the universe should not affect the distance measures significantly. However, the real physical size of the galaxies, d, are deduced from the angular diameter distance, D_A. This is the ratio of the physical size to the angular size, θ, measured across the sky, $D_A = \frac{d}{\theta}$. If θ is in radians d will be in pc. D_A is related to the transverse comoving distance, D_M, as $D_A = \frac{D_M}{1+z}$. For a flat universe the D_M is simply equal to the comoving distance, D_C, which is found from this integral with z' as variable(Hogg 2000):

$$D_C = \frac{c}{H_0}\int_0^z \frac{1}{\Omega_M(1+z')^3 + \Omega_\Lambda} dz' \tag{18}$$

For the flat universe the integral is thus rather simple and easy to calculate only using the redshift z of the object and the chosen cosmological parameters.

C Apparent optical depth method

The optical depth, τ, is a quantative measure of absorption. If a beam of light with initial intensity $I_0(\lambda)$ interfere with an absorbing medium, the resultant intensity $I(\lambda)$ is related to τ as:

$$I(\lambda) = I_0(\lambda)e^{-\tau(\lambda)} \tag{19}$$

But the actual observed intensity, $I_{obs}(\lambda)$, is different than the true $I(\lambda)$, due to a restricting resolution of the instrument. In the measure of the apparent optical depth, τ_a, the limits of the instrument is also taking into account. when the line is fully resolved it is fair to assume that the $\tau_a = \tau_{true}$(Savage & Semback 1991). Since τ is proportional to the column density, $N(\lambda)$, the oscillator strength, f, and the central wavelength, λ_0:

$$\tau(\lambda) \propto f\lambda_0^2 N(\lambda) \tag{20}$$

Thus by integrating the line profile the total column density may be obtained. If the line is not resolved the same equation is valid for τ_a and the apparent column density, $N_a(\lambda)$. The apparent optical depth method works well for unsaturated lines. However, if one observe more than two lines of the same species the difference in the product of $f\lambda_0$ for the two will tell about the level of saturation(Savage & Semback 1991).

D Data Processing

In this section the data processing step to construct the final science/target spectra of the two low redshift galaxies NGC-4193 and UGC-08066 is described.All the necessary data processing was done for the X-shooter Large Programme spectra and was ready to be analysed.
The applied statistics on the spectra are described in the Appendix F.

D.1 The instrument settings and the data

The instrument used for the observations of the two low redshift galaxies is the FORS two on the VLT `http://www.eso.org/sci/facilities/paranal/instruments/fors.html`. An overlook of the data acquired in the end of January 2009 is seen in table D.1. The observation has been done over two sets of dates. There will be refered to the two sets as the first(17th and 18th) and the second set(28th, 29th and 30th). For NGC-4193 two grisms are covering the wavelength interval from 3300 - 8450 Åand the one grism 600RI for UGC-08066 is covering 3300 - 6210 Å.

The slit used has a width of 1.3″. The pixel scale for FORS2 is $0.25''/pixel$, which thus make the slit width 5.2 pixels.

Target	Date	Grism	Seeing	# frames	Exposure time	Avg. Airmass	Data folder
NGC-4193	17th	600RI	0.90-1.02	2	450	1.2785	330845
	18th	600B	0.67-0.69	2	1150	1.312	330840
	18th	600B	0.80-0.81	2	1150	1.312	330844
UGC-08066	27th	600RI	0.92-1.08	2	1500	1.308	330849
	28th	600RI	0.96-1.16	2	1500	1.38255	330848
	28th	600RI	0.93-1.29	2	1500	1.38225	330856
	30th	600RI	0.64-0.89	2	1500	1.3735	330849

Table 3: All the observations was done during January 2009.

FORS2 has two CCD chips. The targets, the galaxy-quasar pairs, are covered using only one of the chips, CHIP1.The data for both chips has been processed, however, since the data for CHIP2 is not used the processing steps explained in this section will focus on CHIP1.

D.2 The calibration frames

ESO provided DVDs with science and the calibration frames. All the nessesary calibration frames was included, bias, flat, lamp and standard star frames, and do not include any darks. The ESO achieves was also searched for extra frames, though none were found which was done in the same period with the same settings.

D.3 Bias Frames

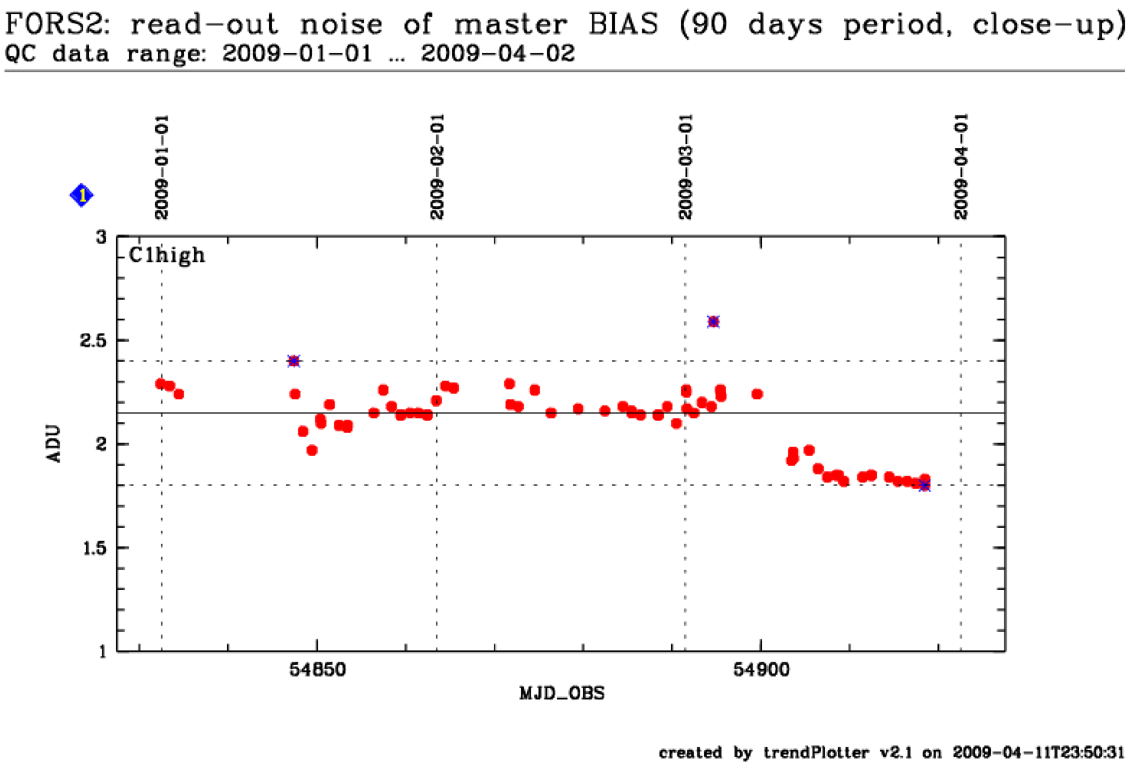

Figure 30: .http://www.eso.org/observing/dfo/quality/FORS2/reports/2009/BIAS_ron_master/trend_report_BIAS_ron_master_2009_1.html

Bias frames was available for each observation date. Therefore there were several combinations which master bias frame(s) might have been constructed from. To make it simple the aim was to investigate if only one master bias frame contructed from the average combinantion of all the frames would work. One might be able to combine bias frames taking with several days interval if the bias level for the CCD has not changed significantly.The bias level might be measured for each of the frames(e.g. one for each night) to determine if the level has changed. The history of the bias level is also stored in the FORS2 archieves, a plot for the observation period is seen in fig 30. The bias level do vary a bit according to the history plot but not significantly. To be certian the small deviations did not affect the master bias, different combinations of frames was average combined and compared. The compared master bias frames compared was one for one day, two for the two sets of days, and one including all frames available. The bias level measured was essentially the same. It was therefore decided to use only the master bias frame contructed from the average combination of all the frames.

D.4 Flat frames

Twwo master flat frames was constructed, one for each of the two grisms applied. It was of course nessesary to fit a wavelength response function in order to normalize in the spectral direction of the 2D spectra. The count level in the spatial direction changed with more than 6 % near the edges of the CCD, probably because the illumination on the CCD/slit have not been very homogenously lit by the flat lamps. Therefore the spatial direction of the CCD was also fitted and normalized. There was fitted polynomial functions with the lowest possible and nessesary in both the spatial and spectral direction. When choosing regions to fit the function to the vignetted corners was avoided.

D.5 Wavelength calibration

The wavelength calibration was applied for the 2D spectra. All the nessesary lamp frames for each of the observation nights was applied along with the science data.

D.6 Cosmic rays corrections

The IRAF procedure lacos_spec.cl[4] was applied in order to correct for the disturbunce on the CCD caused by hits of cosmic rays, cosmics.

The cosmic rays correction is not suffient to correct all the affected pixels for the very contaminated frames. In spectra where a great number of long exposure frames are combined into one there are still several affected pixels which is not corrected.There were e.g. many cosmic ray hits visible in the frames for UGC-08066 due to the long exposures. Different sigma-clippings was tested in order to correct as many cosmics as possible. However, it appeared as if the emission lines also was affected when using a lower sigma-clipping. To be sure that none of the emission lines would be 'corrected' by the algorithm as well a lower sigma-clipping was not applied, eventhough it might have removed more cosmics.

D.7 Combining spectra

The spectra are combined with a variance weigted mean. This is easily done using the target and variance frames. The result of combining the spectra are two spectra for NGC 4193, one for each of the grisms, and one spectra for UGC-08066 combined from all the frames for all dates.
It was considered excluding some of the data for UGC-08066 since the resultant combined spectra containing all the frames resulted in a spectrum still containing many cosmics and bad pixels, it also showed a lower flux level than if just using the data from the 30th. It was tested if using only the data from the 30th would give a better final spectra since it was observed under better conditions/lower seeing than for the previous nights. However, the S/N for the spectra combined for all data is higher than when using only data from the one date. Therefore the combined spectra for UGC-08066 is constructed from the spectra for all dates.When combining the 2D spectra it is important that the targets are placed exactly the same place in the frame. The slit placement has been shifted for each new exposure in order to avoid bad pixels. The targets are positioned upon the slit is found by fitting a Gaussian and measure the central wavelength of a point source. The quasar in the same frame is the measured point source.

D.8 Sky subtraction

As much sky region as possible is chosen when doing the sky subtraction to lower the error which is also added when subtracting the overall sky level and skylines(see Appendix F.1.4). The 'dark' upper corners of the spectrum is avoided, thus a larger number of rows,$\hat{j}$, is selected in the central part than near the edges of the spectrum, see figure 31. Therefore the variance in the middle part of the spectrum should be lower than the variance near the edges.

It was chosen to take the mean of the rows, j, when subtracting the sky, to avoid having an effect from possible still present cosmic ray hits and bad pixels. The mean is calculated and

[4] `http://www.astro.yale.edu/dokkum/lacosmic/`

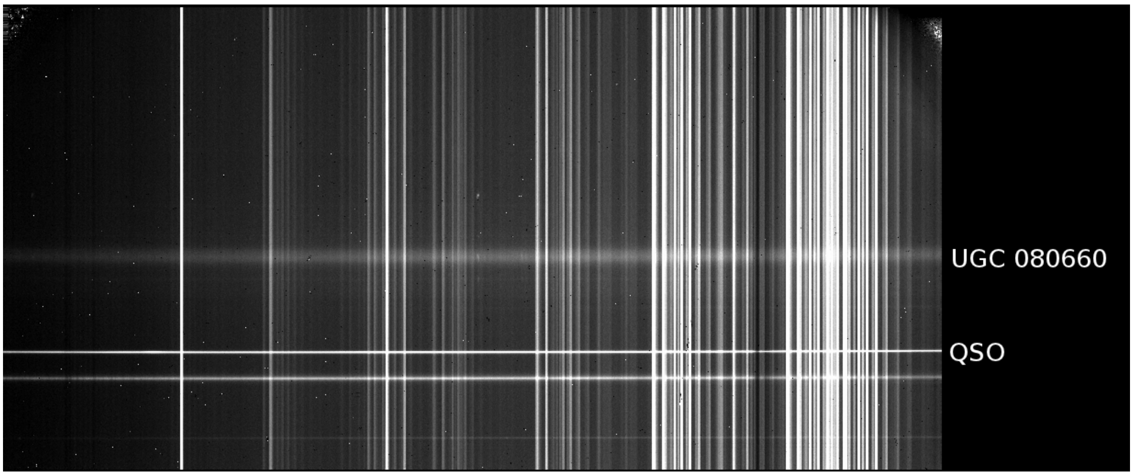

Figure 31: `.A2DspectrumofUGC-08066beforeskysubtraction.`

subtracted for each column, i, and the sky subtracted frame, $S(i,j)_{no\,sky}$,is therefore as so:

$$S(i,j)_{no\,sky} = S(i,j)_{with\,sky} - \frac{1}{\hat{j}} \sum_{j} S(i,j)_{with\,sky} \tag{21}$$

In frames where there are a lot of skylines(the reddest part of the spectrum), there is still residuals from the lines left. Luckily the very domininant lines is not close to any lines used in the analysis and easily avoided.

D.9 Final processed 2D spectra

Here is presented the final processed two dimensional spectra. In figure FIGURE is the two spectra for NGC-4193, covering the wavelength range 3500 - 8450 Å. In figure FIGURE the one grism for UGC-08066 is seen, it covers 3300 - 6210 Å.

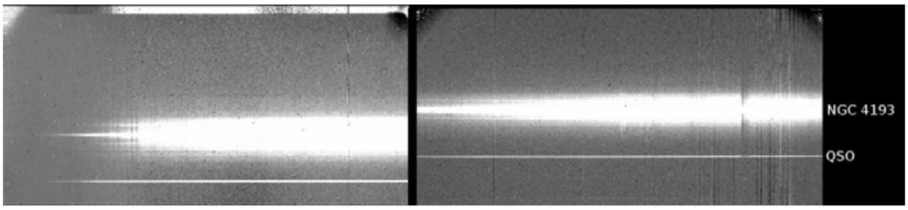

Figure 32: This is the two dimensional spectra for UGC-08066 and the background quasar.

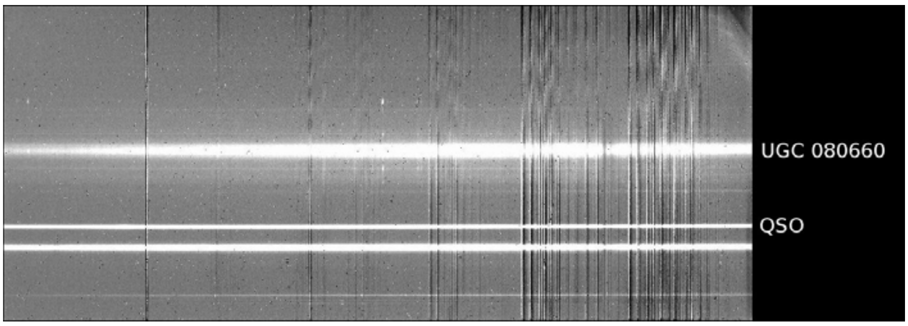

Figure 33: This is the two dimensional spectra for UGC-08066 and the background quasar. In the middle of the spectra the measured Hα and [N II] line is present. To the far left, near the edge of the image [O III] 5007 line is also seen.

D.10 Extracting one dimensional spectra

First the quasar spectra was extracted from the 2D spectra. The trace fit across the CCD is best contructed from a point source. The same fit is therefore applied for the rest of extracted spectra across the galaxy in the same 2D spectrum.

D.11 Apertures across the galaxies

D.11.1 Placement and centre of the galaxy

To be able to compare different grisms with each other it was necessary that the apertures was chosen to be at the same position across the galaxy. Deciding where the centre of the galaxy is by only looking at the long slit spectra is not easy to do precisely by just considering the galaxy spectra. One might e.g. decide that the centre is where the highest flux near is observed, however, this might not be exactly the same for different wavelength and thus not the same grisms. Therefore instead of having the galaxy centre as a reference point when placing the apertures a point source was chosen instead. The obvious point sources to choose as reference points are of course the position of the quasars since the spectra of these has been made. This also conveniently gave the distance from the quasars to the centre of the galaxies, which have been converted to arc seconds via the detector pixel scale($0.25''/pixel$) and afterwards to kiloparsec,REFER TO SECTION/APPENDIX. The distance between UGC 08066 is (463.5-257=) 206.5 pixels.

D.11.2 Size

The aperture sizes was chosen so the resultant S/N of the measured line ratios would be above approximately 5. However, the spectra has in the central part high enough flux/counts to only be contained in an aperture of the size of one pixel. The minimum size used as an aperture is determined from the fact that it should be larger than the seeing. The seeing in the header was the value which set the lower limit of the apertures. However, the seeing was also measured from the data as the FWHM of the quasar, measure by a Gaussian fit in the 2D spectra in the spatial direction. The FWHM/seeing was measured for wavelengths near the analysed emission lines. For all the spectra the different exposures have slightly different seeing according to the header and the maximum seeing was the one chosen to set the lower limit. To convert from the seeing measured in arcseconds to pixels the detector pixel scale($0.25''/pixel$) is used. Thus the minimum size for NGC 4193 using grism 1 is 4 pixels, using grism 2 is 4 as well and for UGC 08066 it is 5 pixels. The measured seeing is actually much higher, approximately twice as high as the values taken from the headers. This means that the apertures chosen overlap, and that the measured parameters measured in neighbouring apertures are correlated.

D.12 Flux calibration

There have been observed standard stars for all grisms, three for grism 600RI(18th, 28th and 29th), since it is used with several days of separation. Only two of the standard stars for grism 600RI is used, the one for the 18th and the 29th. The flux calibration data for 18th is applied to the combined spectra for NGC 4193 grism 600RI, and the data for the 29th for UGC 08066 since it is the middle date/closest date for the observation dates of the target.
Since the spectra was average combined before the flux calibration the average airmass measured for all the combined spectra is applied in the calibration.

Grism 600B is in the blue end of the spectrum, and the sensitivity in the UV(below 3500 Å(LOOK AT SPECTRUM!) is very low compared to the higher wavelengths. This made it difficult to fit a function, since the sensitivity transition at the point is not very continuous. The necessary emission lines are at higher redshift and therefore it was chosen not to fit to the lowest wavelengths for grism 600B.

D.13 Extinction correction

In order to correct for extinction due to the dust in the Milky Way, Galactic extinction, the colour excess, E(B-V), is found towards in the observed sight-lines via a galaxy sky map of E(B-V)[5]. The sky map is in galactic coordinates which is converted to from the right ascension, RA, and declination, DEC, of the two galaxy centre. The RA and DEC is given in the header of the files(keyword: (J2000) pointing) as listed in table 4. The angular distance between the quasars and the galaxies are quite small, so only one value for each galaxy-QSO pair is applied.

Object	RA,DEC	longitude,latitude	E(B-V)
NGC-4193	183.453740,13.17538	268.84674,73.504928	0.0301918
UGC-08066	194.268210,1.03451	306.13155,63.871247	0.0173608

Table 4:

[5] `http://www.astro.princeton.edu/~schlegel/dust/data/data.html`

This value of extinction/redenning, E(B-V), is an input in the IDL procedure fm_ unred.pro[6], which dereddens the flux by applying Fitzpatrick 1999 parameterization. This is valid for late-type galaxies.

E The quasar spectra

The resultant quasar spectrum near the sight-line of NGC-4193 is shown in fig 34. Here it is obvious that the flux is not correct for all grisms, since there is not same flux level where the grisms overlap. This might be slitloss caused by the slit not being aligned at precisely the same position for all the exposures.
When comparing with a quasar template it is evident that only the broad emission line MgII is the only measurable quasar line in the spectra. There was searched for absorption lines which could be caused by the intervening galaxy NGC-4193. None of the possible absorption lines are significant enough to be measured, though a hint of absorption due to CaII $\lambda3934$,$\lambda3969$ is seen in the spectrum if zoomed in, see figure 35.

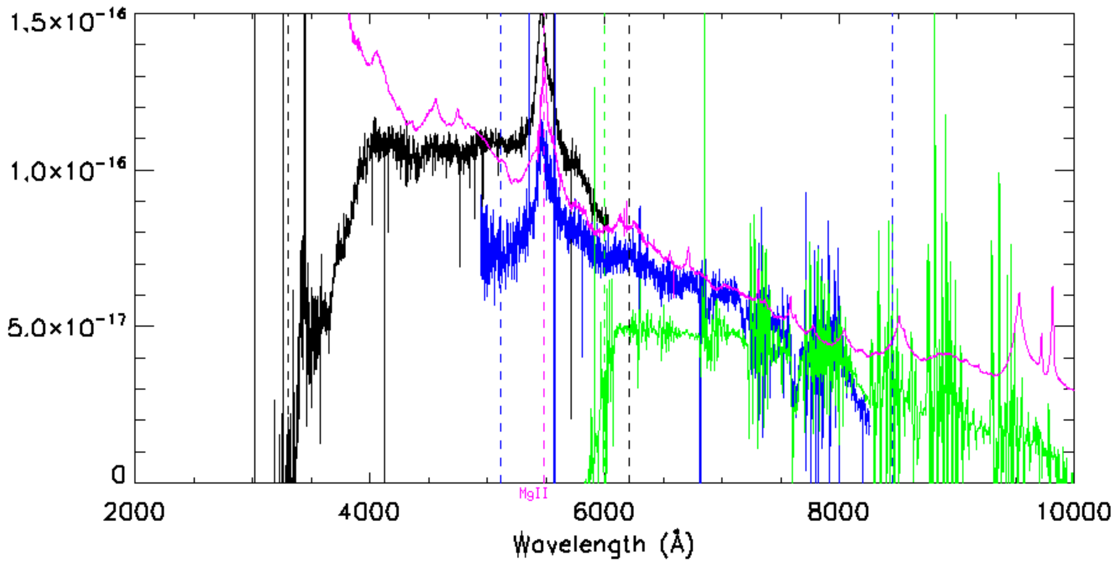

Figure 34: NGC-4193: This is the spectra of the background quasar. The three spectra from each of the three grisms are represented in the colours black, blue and green. The vertical dashed lines in the same colour indicate which wavelength the grisms should cover according to the FORS2 website. The magenta coloured spectrum is a quasar template to compare with. The magenta vertical dashed line marks the Mg II emission line.

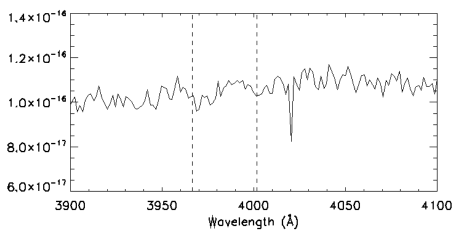

Figure 35: NGC-4193: This is the spectra of the background quasar. The vertical dashed lines in the same colour indicate where the possible doublet absorption line, Ca II $\lambda3934$,$\lambda3969$, for NGC-4193 would be at the redshift of the galaxy. As can be seen there is a hint of these lines.

The quasar spectrum near the sight-line of UGC-08066 is shown in fig 36. As is seen for NGC-4193 the broad emission MgII line is visible. There are no absorption line which could be caused by the galaxy present in the spectrum. However, they might still be present in the ultra-violet wavelength regime.

[6] `http://idlastro.gsfc.nasa.gov/ftp/pro/astro/fm_unred.pro`

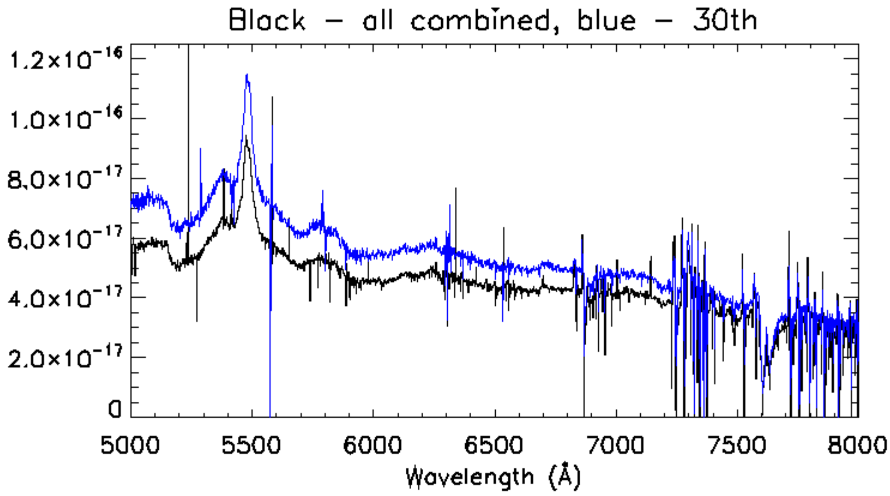

Figure 36: UGC-08066: This is the spectra for the backgorund quasar. The black line is the spectrum for all the frames combined, while the blue spectrum is only data from the 30th of January 2009.

F Statistics

In this section is explained some of the statistics used in both the processing and analysis of data. If the statistics is not specifically explained in this section the simplified error propagation is used in the form of the variance formula.

F.1 2D Variance spectra

F.1.1 Basic data processing steps

Two dimensional variance spectra was created by applying error propagation for all the processing steps and by the use of Poisson statistics. In Poisson statistics one may simply add the errors/variance, which makes this process relatively simple Poisson statistics apply for photons/electrons, which is why all the calculations of adding the errors is done in counts of electrons/counts on the CCD. Therefore there is converted to electrons when nessesary by using the gain of the detector($gain = 0.6993ADU/e-$).
The read noise, RON is the noise floor all the frames. The RON is 2.9 ADU for chip 1 for the specific settings used for these longslit spectra. A basis variance spectrum/variance 'floor' is the RON squared.
First of all when subtracting the master bias frame an error, in the form of the variance σ^2_{bias} is added to the RON:

$$\sigma^2_{bias} = \frac{RON^2}{\#bias\,frames} \tag{22}$$

The number of bias frames used is 20 for chip 1. The variance for the master flats are dependent on the number of flat frames and the average flat level $< flat\,level >$:

$$\sigma^2_{flat} = RON^2 + \sigma^2_{bias} + "\frac{RON^2}{'\#flat\,frames' \cdot < flat\,level >^2} + \frac{'master\,bias'}{'\#flat\,frames' \cdot < flat\,level >} \tag{23}$$

When dividing by the master flat and subtractincg the bias the equation for the variance for the processed target spectrum, S, is:

$$\sigma^2_S = \frac{S + RON^2 + \sigma^2_{bias} + S^2\sigma^2_{flat}}{'MasterFlat'^2} \tag{24}$$

There is not calculated/added any error from the wavelength calibration.

F.1.2 Cosmic rays corrections

What it essentially done when correcting for cosmic rays(very high outliers) is simply a value subtracted at the pixel values where the cosmic rays have hit the CCD. Thus it is quite simple to add the error in the variance spectrum. What is done to correct the pixels influenced by the cosmic rays might be seen as multiplying with a factor, F_{cm}. Thus the variance image, σ^2_{prev}, should also just be multiplied with that factor squared.

When correcting for cosmics in a 2D spectrum with the IRAF procedure *lacos_spec.cl* the output is a 2D spectrum with the removed cosmics, $S_{no\,cm}$, and a mask/map, $mask$, of zeroes and values of one, where the ones indicate where a cosmic has been removed. Thus a frame containing the factors, f_{cm}, for each pixel which the original spectrum, S_{cm} has been multiplied with is $f_{cm} = \frac{S_{no\,cm}}{S_{cm}} \cdot mask$. There is multiplied with the mask in order to only add the error for pixels corrected for the cosmics. Thus the new variance calculated is: $\sigma^2_{no\,cm} = \sigma^2_{previous} + \sigma^2_{cm} \cdot f^2_{cm}$.

F.1.3 Combining spectra - variance weigted mean

In order to make the process of combining the 2D spectra simple there is not combined more than two spectra at once. This also makes it easier to be sure that the spectra overlap correctly for another spectra is combined. The combination of the spectra is done using a variance weigted mean, which for two spectra, $S1$ and $S2$, with corresponding variance spectra, $V1$ and $V2$, appear as so :

$$S12 = \frac{S1 \cdot V2 + S2 \cdot V1}{V1 + V2} \tag{25}$$

The two variance spectra, $V1$ and $V2$, are combined into the new variance spectrum, $V12$, as:

$$V12 = \frac{V1 \cdot V2}{V1 + V2} \tag{26}$$

The same formulas are used several times if more than two frames is to be included in the final 2D spectra.

F.1.4 Sky subtraction

The sky values which are subtracted are the median of the rows, j, chosen of the sky background. This is done for each columnm, i. When using the median a factor of $\frac{\pi}{2}$ is multiplied to the variance. The variance is also divided by the number of rows which are median combined, $\hat{j}$ and squared[7]:

$$\sigma(i,j)^2_{sky} = \frac{1}{\hat{j}^2} \sum_j \sigma(i,j)_{previous} \tag{27}$$

This variance is just added to the previous.

F.1.5 Flux calibration

There is not calculated nor propagated an error caused by the flux calibration, meaning that the exact same calibration are used on the variance spectra as for the target spectra. However it is important to remember to take the square root of the variance and use the standard deviation, σ, as the error and convert σ from electrons to $ergs/sec/\AA$.

F.2 Stellar absorption correction

The simplified error propagation law is applied in order to calculate the errors on the flux values when subtracting a Gaussian. The errors on the Gaussian fit is an output when using the IRAF procedure $ngaussfit$. The procedure also accounts for the errors in the spectrum when an error spectrum is included in the input file. The input file should simply contain the wavelengths, fluxes and the standard deviations of the flux.

F.3 Voigt fitting - χ^2

The definition of the reduced χ^2 is:

$$\chi^2 \equiv \frac{1}{\Gamma} \sum_{i=1}^{\nu} \frac{(x_i - \mu_i)^2}{\sigma_i^2} \tag{28}$$

The sum is over the all the fit points chosen for the Voigt profile fitting. The variables are as follows:

[7]The equation is from lecture notes from a course, *Astronomical Data Processing*, provided by the University of Copenhagen. The notes are written by Peter Jakobsen

- ν - Number of independent variables, in this case number of points chosen to make the fit from
- x - Measured spectral values
- σ - The standard deviation
- μ - Values for the fit
- Γ - number of degrees of freedom: $\Gamma = \nu - n$, where n is the number of fitted paramaters, for the voigt profile fitting it is 1 - the column density of neutral hydrogen N_{HI}

All the reduced chi-squared values calculated for the Voigt profile is above 1, some of the values actually being far above, meaning that the fit to the data is not very significant. The large χ^2 values are, however, for most fits probably due to a wrong/bad continuum fit. The continuum is therefore often redone several times before a proper fit is made. As previously explained in 16.2 the continuum fitting is not trivial, and the continuum fits are easily not the best representation of the real underlying quasar spectrum.

F.4 Ω_g^{DLA}

The standard error for N_{tot} might be given as a standard deviation for the summed sample of m column densities, $N_{HI,i}$, with sample mean $< N_{HI} >$ (Lanzetta et al. 1999, page 50):

$$\sigma_{N_{tot}} = \frac{1}{(1-1/m)^2} \frac{\sqrt{\Sigma_i (N_{HI,i} - < N_{HI} >)^2}}{\Delta X} \tag{29}$$

This error for N_{tot} is propagated through equation 6 to give the 1σ uncertainty on Ω_g^{DLA}.

F.5 Equivalent width

The 1σ upper level on the digital equivalent width, σ_{EW}, is[8]:

$$\sigma_{EW}^2 = \sum_{\lambda_1}^{\lambda_2} \left(\frac{\Delta\lambda}{F_\lambda}\right)^2 \sigma_F^2 = \left(\frac{\lambda_2 - \lambda_1}{n_\lambda}\right)^2 \sum_{\lambda_1}^{\lambda_2} \left(\frac{\sigma_F}{F_\lambda}\right)^2 \tag{30}$$

If the spectrum is normalized to the continuum the variance for the flux, σ_F^2 should be as well. There is not assumed an error of the continuum fitting and therefore σ_F^2 is simply normalized to the same function as the spectral values, F_λ.

[8]The equation is from lecture notes from a course, *Astronomical Data Processing*, provided by the University of Copenhagen. The notes are written by Peter Jakobsen)

G Figures

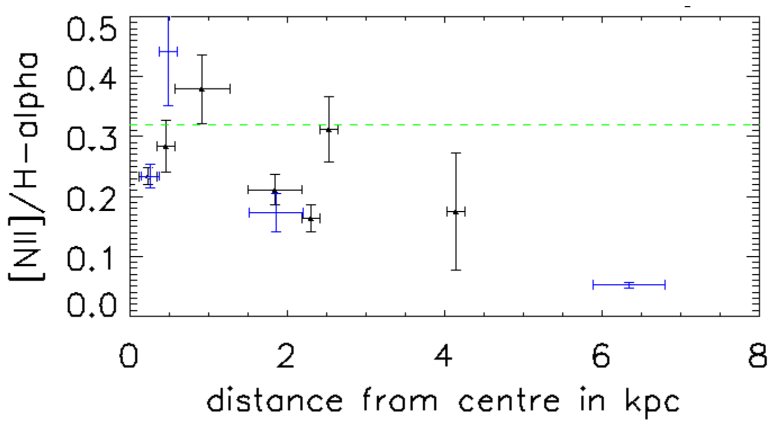

Figure 37: UGC-08066. This plot shows N2 index measured for both sides of the galaxy. The black points indicate the metallicity in the direction of the quasar sight-line and the blue points indicate the metallicity in the opposite direction.

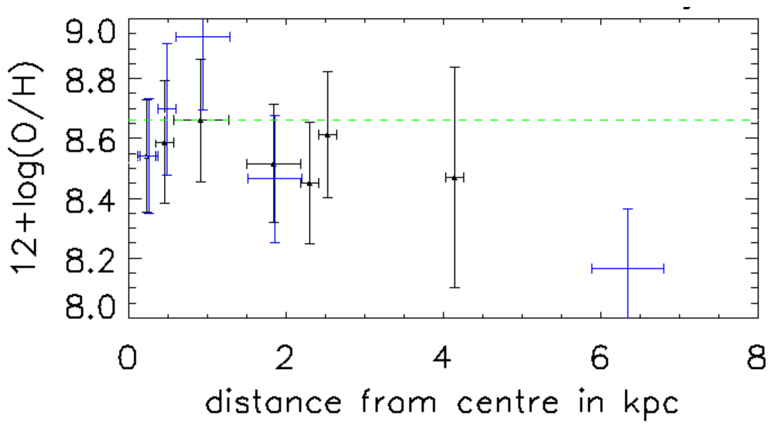

Figure 38: UGC-08066. This plot shows the metallicity measured via the $N2$ index. The black points indicate the metallicity in the direction of the quasar sight-line and the blue points indicate the metallicity in the opposite direction of the quasar incident point.

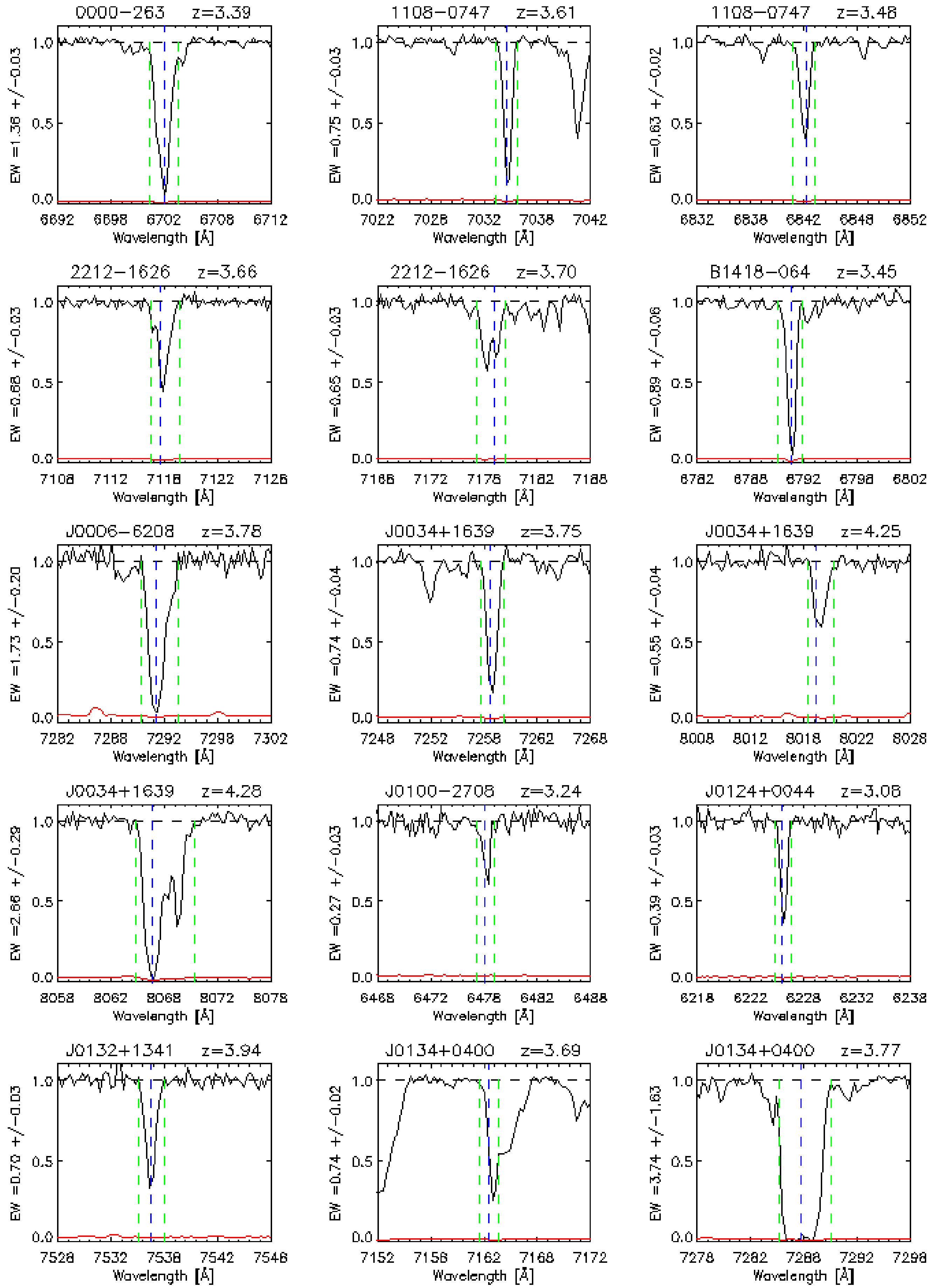

Figure 39: Plots of measured equivalent widths, $EW's$, of Si II 1526. The blue dashed lines indicate the measured redshift for the absorbers. The green dashed lines mark the minimum and maximum wavelengths for which $EW's$ was measured using equation 16.

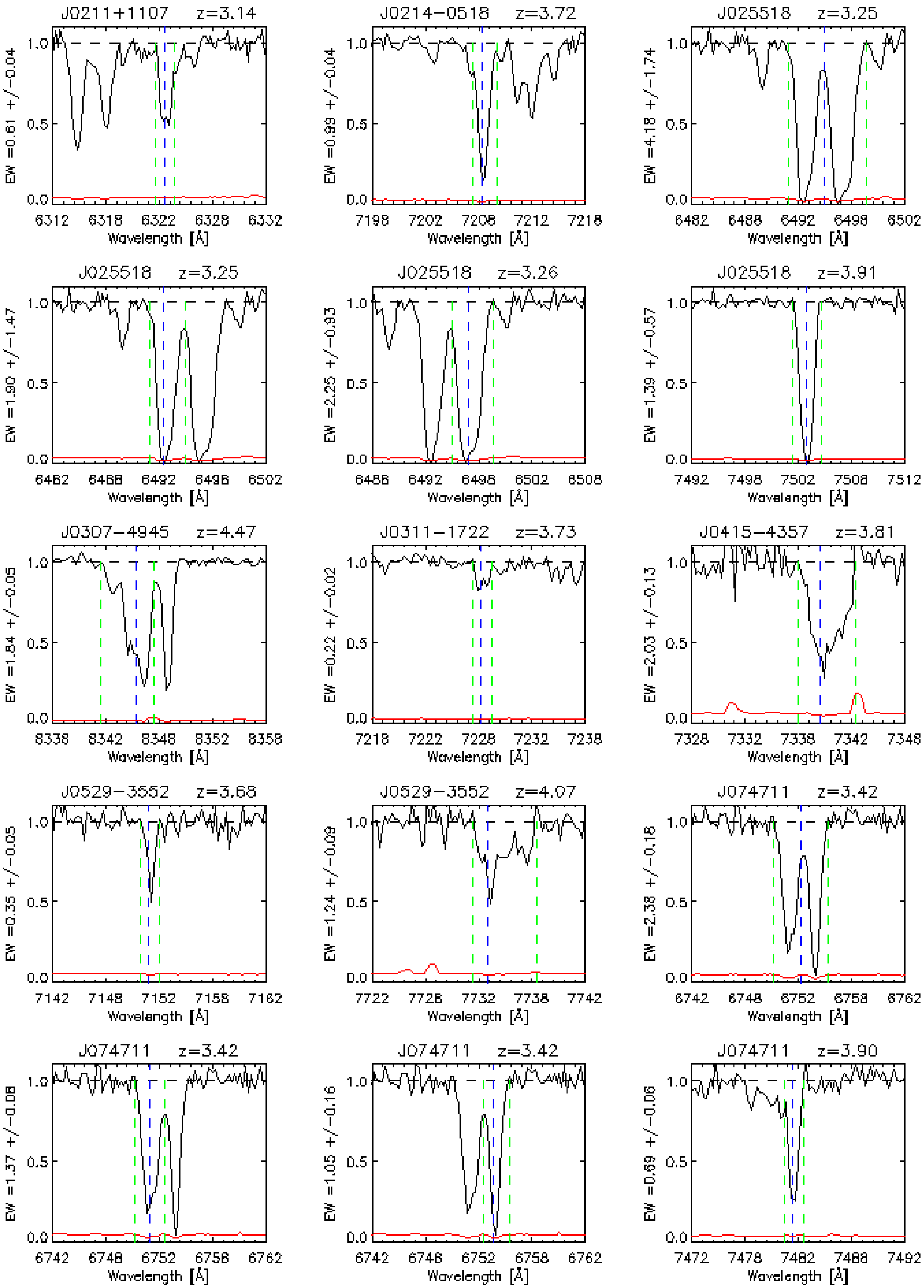

Figure 40: Plots of measured equivalent widths, $EW's$, of Si II 1526. The blue dashed lines indicate the measured redshift for the absorbers. The green dashed lines mark the minimum and maximum wavelengths for which $EW's$ was measured using equation 16.

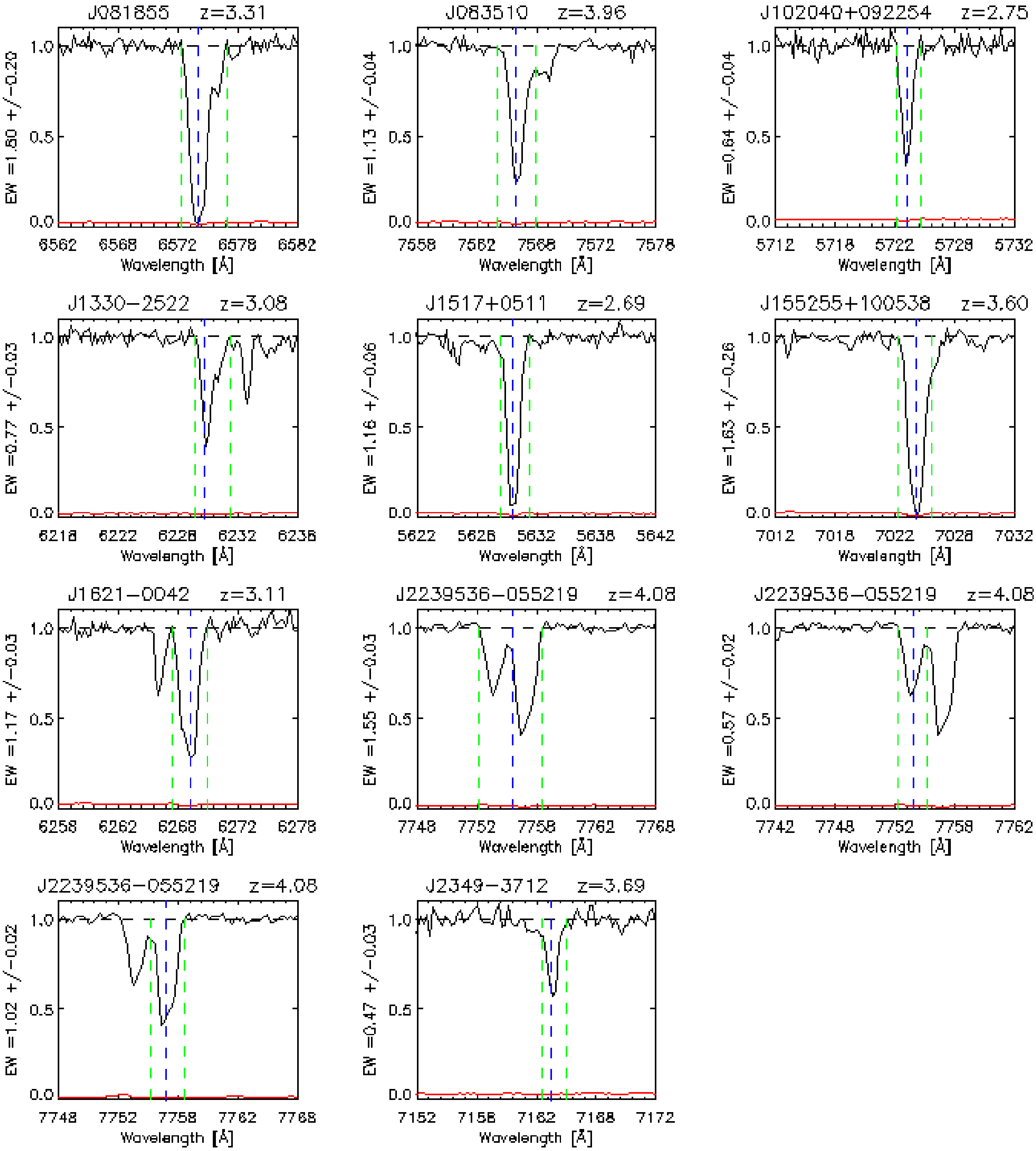

Figure 41: Plots of measured equivalent widths, $EW's$, of Si II 1526. The blue dashed lines indicate the measured redshift for the absorbers. The green dashed lines mark the minimum and maximum wavelengths for which $EW's$ was measured using equation 16.

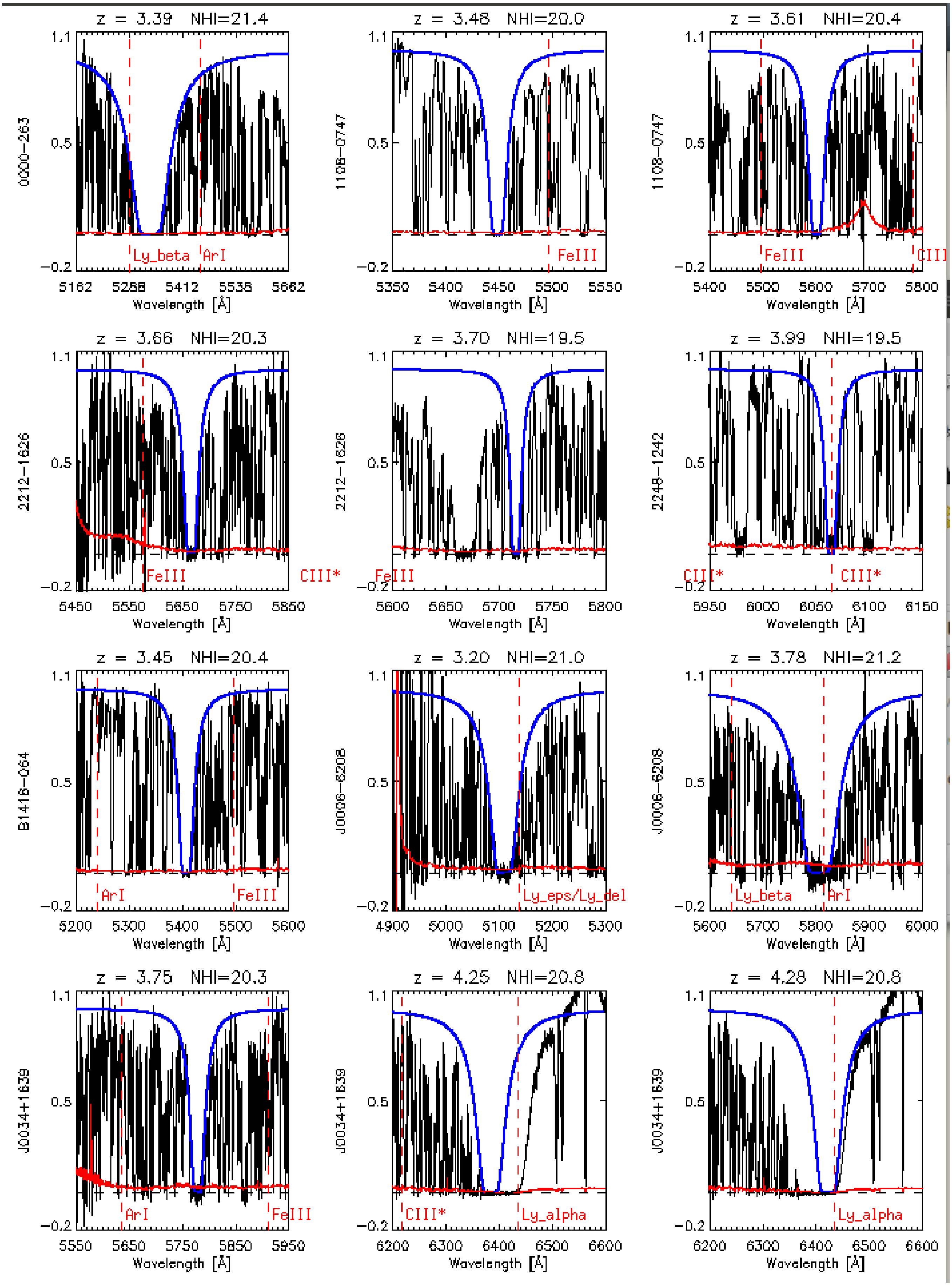

Figure 42: Here are twelve of the Voigt fits(blue line) for the DLAs, the redshift for the absorbers are typed in the title. The spectra are normalized. The vertical dashed red lines marks the central wavelength for the QSO emission lines. The NHI values are the column densities, N_{HI}, in units of dex

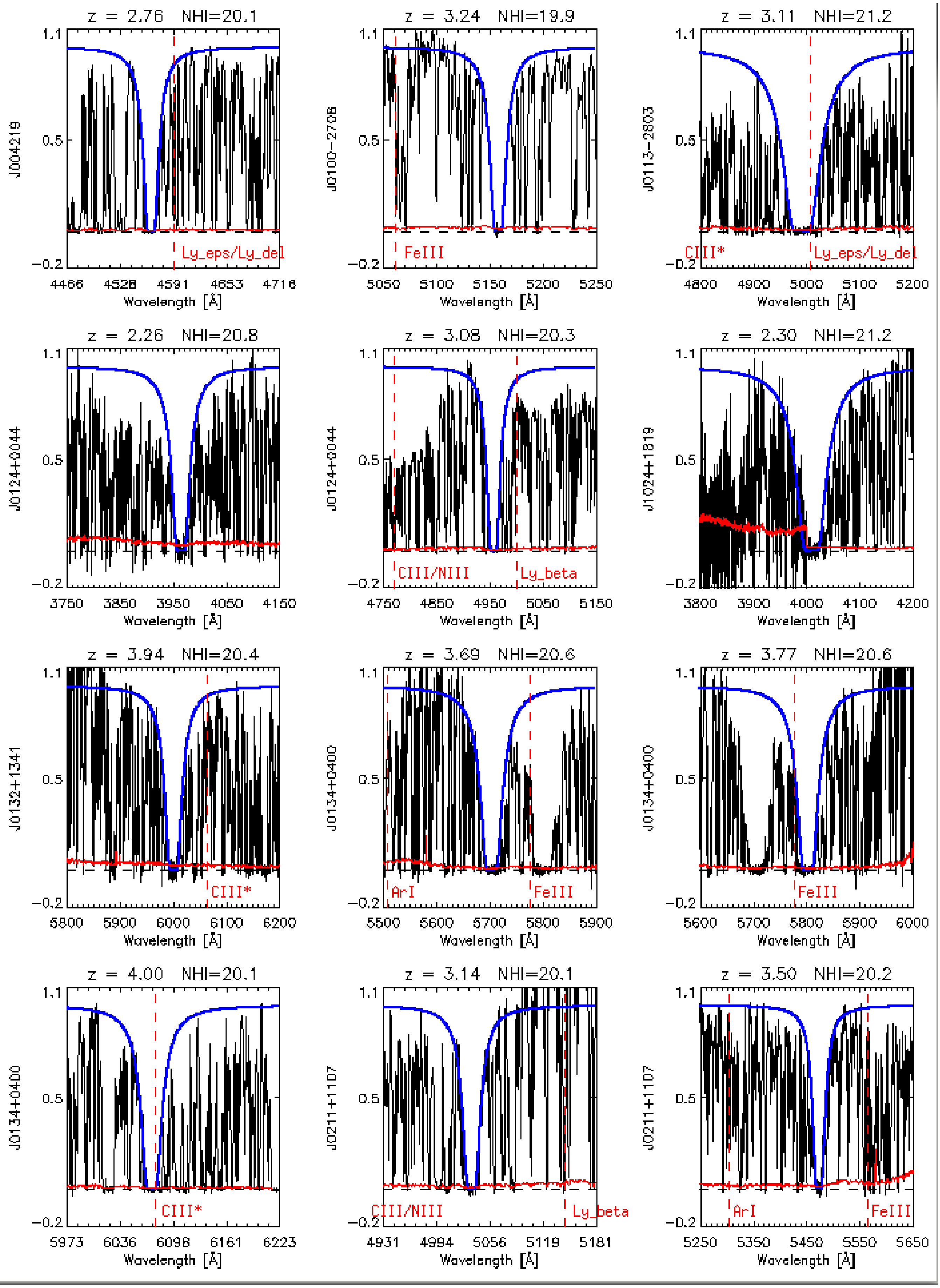

Figure 43: Here are twelve of the Voigt fits(blue line) for the DLAs, the redshift for the absorbers are typed in the title. The spectra are normalized. The vertical dashed red lines marks the central wavelength for the QSO emission lines. The NHI values are the column densities, N_{HI}, in units of dex

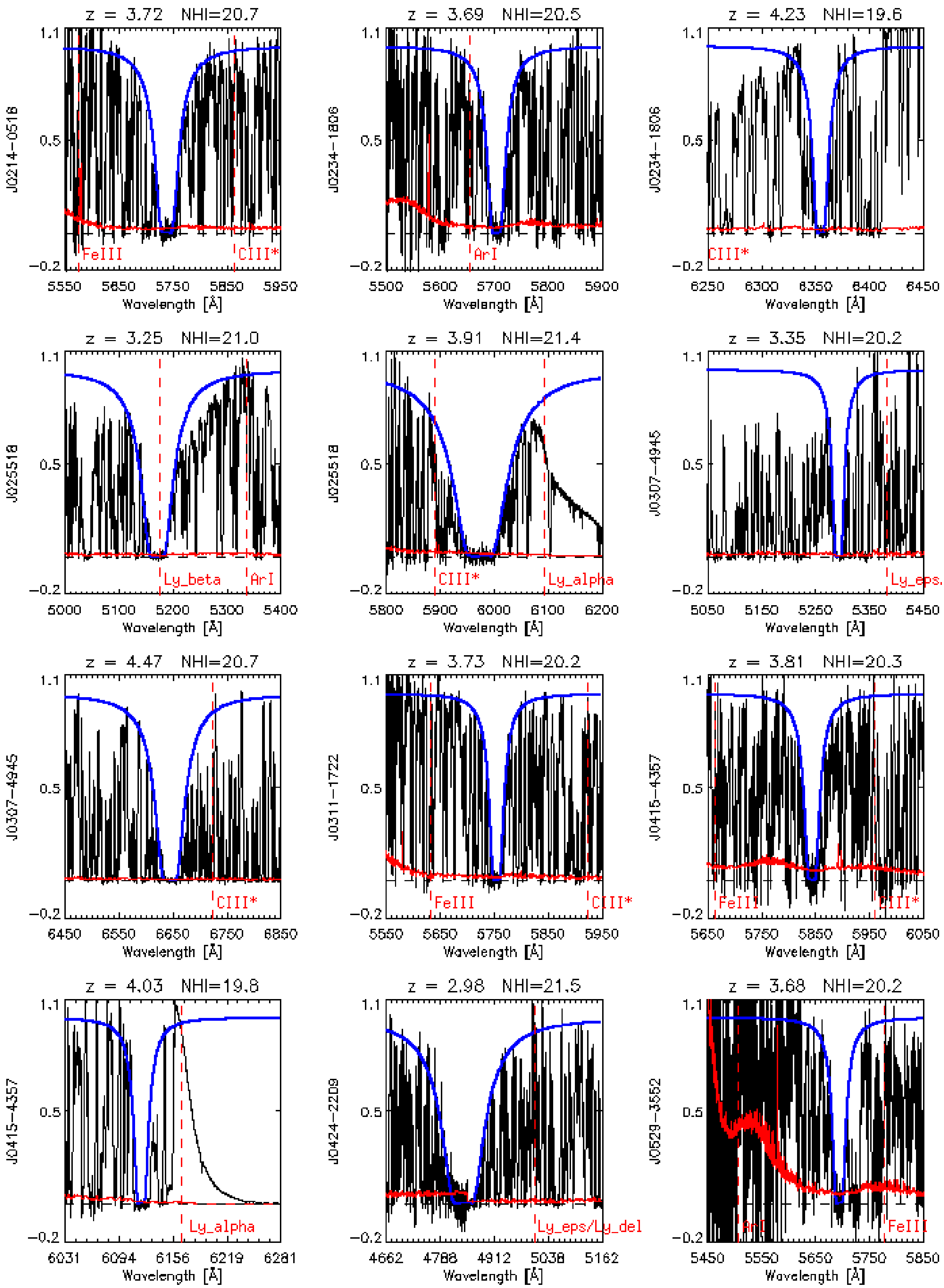

Figure 44: Here are twelve of the Voigt fits(blue line) for the DLAs, the redshift for the absorbers are typed in the title. The spectra are normalized. The vertical dashed red lines marks the central wavelength for the QSO emission lines. The NHI values are the column densities, N_{HI}, in units of dex

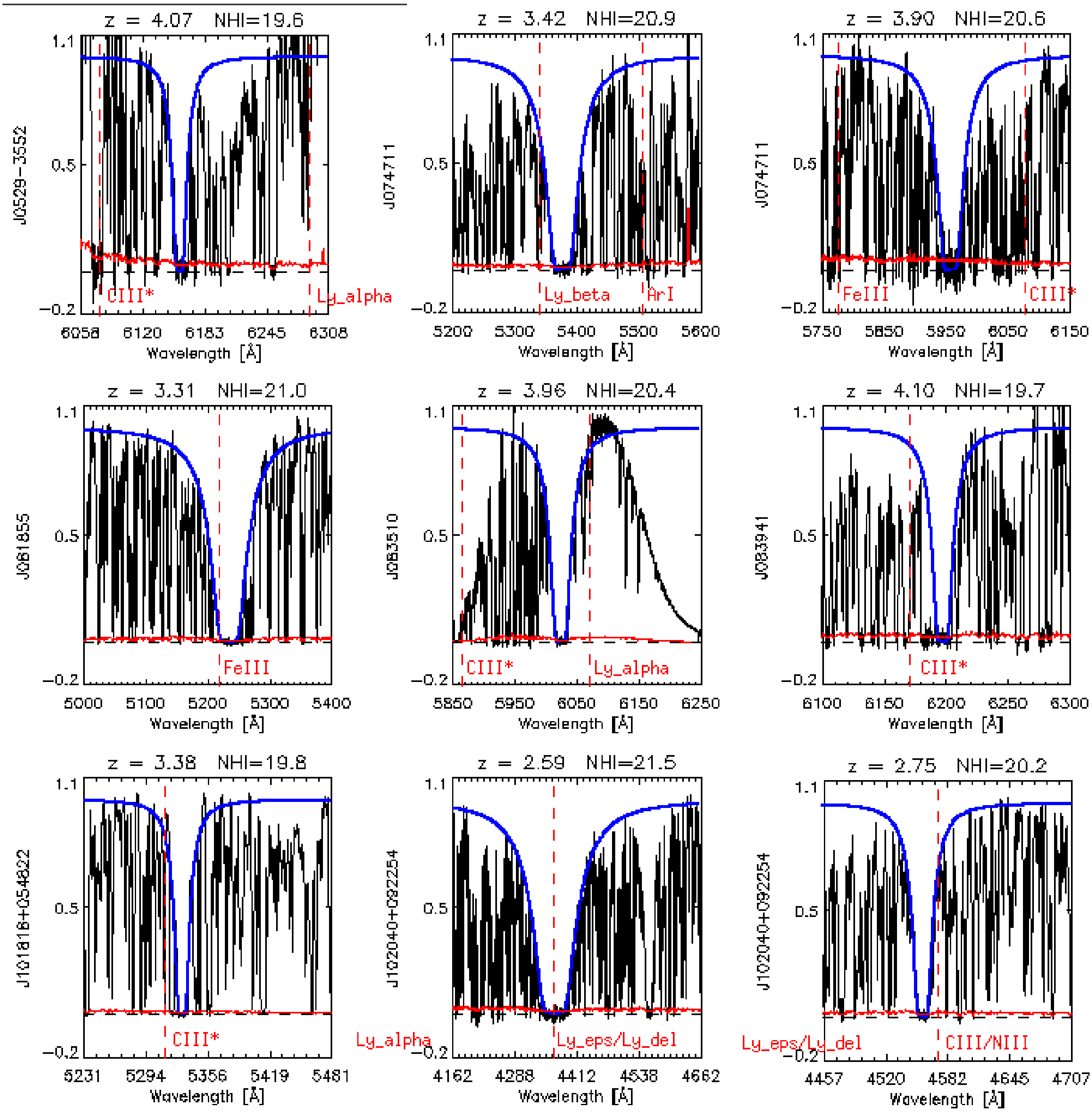

Figure 45: Here are twelve of the Voigt fits(blue line) for the DLAs, the redshift for the absorbers are typed in the title. The spectra are normalized. The vertical dashed red lines marks the central wavelength for the QSO emission lines. The NHI values are the column densities, N_{HI}, in units of dex

H DLA table

QSO ID	z_{qso}	z_{dla}	N(HI) dex	EW_{1526} Å	σ_{EW} Å	[M/H] dex
°0000-263	4.12	3.390	21.4	1.36	0.03	-1.6
1108-0747	3.92	3.482	20.0	0.75	0.03	-2.0
°1108-0747	3.92	3.608	20.4	0.63	0.02	-2.1
2212-1626	3.99	3.662	20.3	0.68	0.03	-2.1
2212-1626	3.99	3.702	19.5	0.65	0.03	-2.1
2248-1242	4.16	3.989	19.5			
°B1418-064	3.92	3.448	20.4	0.89	0.06	-1.9
J0006-6208	4.46	3.203	21.0			
°J0006-6208	4.46	3.776	21.2	1.73	0.20	-1.5
J0034+1639	4.29	3.754	20.3	0.74	0.04	-2.1
**J0034+1639	4.29	4.252	20.8	0.55	0.04	-2.3
**J0034+1639	4.29	4.284	20.8	2.66	0.29	-1.3
J004219	3.88	2.755	20.1			
J0100-2708	3.53	3.243	19.9	0.27	0.03	-2.6
J0113-2803	4.32	3.106	21.2			
J0124+0044	3.84	2.261	20.8			
J0124+0044	3.84	3.078	20.3	0.39	0.03	-2.4
J1024+1819	3.53	2.298	21.2			
°J0132+1341	4.16	3.936	20.4	0.70	0.03	-2.1
°J0134+0400	4.17	3.692	20.6	0.74	0.02	-2.1
°*J0134+0400	4.17	3.772	20.6	3.74	1.63	-1.1
J0134+0400	4.17	3.996	20.1			
J0211+1107	3.98	3.142	20.1	0.61	0.04	-2.1
*J0211+1107	3.98	3.502	20.2			
°J0214-0518	3.99	3.721	20.7	0.99	0.04	-1.9
°J0234-1806	4.31	3.693	20.5			
J0234-1806	4.31	4.228	19.6			
°*J025518	4.01	3.254	21.0	4.18	1.74	-0.9
**J025518	4.01	3.253		1.90	1.47	-1.4
**J025518	4.01	3.255		2.25	0.93	-1.3
°J025518	4.01	3.915	21.4	1.39	0.57	-1.7
J0307-4945	4.72	3.354	20.2			
°J0307-4945	4.72	4.466	20.7	1.84	0.05	-1.6
J0311-1722	4.04	3.734	20.2	0.22	0.02	-2.8
J0415-4357	4.07	3.807	20.3	2.03	0.13	-1.4
J0415-4357	4.07	4.034	19.8			
J0424-2209	4.32	2.983	21.5			
J0529-3552	4.17	3.684	20.2	1.24	0.09	-1.7
J0529-3552	4.17	4.065	19.6	0.35	0.05	-2.5
*J074711	4.17	3.423	20.9	2.38	0.18	-1.3
** J074711	4.17	3.422		1.37	0.08	-1.6
** J074711	4.17	3.424		1.05	0.16	-1.8
°J074711	4.17	3.901	20.6	0.69	0.06	-2.1
J081855	3.67	3.306	21.0	1.80	0.20	-1.5
J083510	3.99	3.956	20.4	1.13	0.04	-1.8
J083941	4.25	4.098	19.7			
J101818+054822	3.52	3.385	19.8			
J102040+092254	3.64	2.593	21.5			
J102040+092254	3.64	2.749	20.2	0.64	0.04	-2.0
J1330-2522	3.95	3.080	19.9	0.77	0.03	-1.9
J1517+0511	3.56	2.688	21.4	1.16	0.06	-1.6
°J155255+100538	3.73	3.601	21.0	1.63	0.26	-1.6
*J155255+100538	3.73	3.667	20.6			
J1621-0042	3.70	3.106	19.9	1.17	0.03	-1.7
J163319+141142	4.33	2.594	20.4			
°*J2239536-055219	4.56	4.080	20.6	1.55	0.03	-1.6
**J2239536-055219	4.56	4.079		0.57	0.02	-2.3
**J2239536-055219	4.56	4.081		1.02	0.02	-1.9
°J2344+0342	4.24	3.220	21.2			
J2349-3712	4.21	3.692	20.2	0.47	0.03	-2.3

Table 5: Here is data for all the DLAs and sub-DLAs identified in the X-shooter quasar sample. EW_{1526} is the measured which should be in the rest frame in order to convert to the metallicity, [M/H]. The 1σ value for [M/H] is mainly due to the conversion from EW_{1526} and all the measurements of [M/H] has $\sigma_{EW} \approx 0.3$ dex. The absorbers marked with was observed as possible two absorbers and the absorbers marked as are one of the these two absorbers. The ° marks the DLAs which are applied to calculate Ω_{DLA}